INTERNATIONAL JOURNAL FOR NUMERICAL METHODS IN FLUIDS
Int. J. Numer. Meth. Fluids 2005; **49**:233–266
Published online 23 May 2005 in Wiley InterScience (www.interscience.wiley.com). DOI: 10.1002/fld.988

Dendritic solidification of binary alloys with free and forced convection

P. Zhao[1,*,†] J. C. Heinrich[1,‡] and D. R. Poirier[2,§]

[1]*Department of Mechanical Engineering, The University of New Mexico, Albuquerque, NM 87131, U.S.A.*
[2]*Department of Materials Science and Engineering, The University of Arizona, Tucson, AZ 85721, U.S.A.*

SUMMARY

Dendritic solidification with forced convection and free convection driven by contraction and thermo-solutal buoyancy is simulated in two-dimensional space using a sharp-interface model. Both pure substances and alloys are considered. The model is formulated using the finite element method and works directly with primitive variables. The coupled energy- and solutal concentration-equations, along with the Navier–Stokes equations for incompressible flow, are solved using different meshes. Temperature is solved in a fixed mesh that covers the whole domain (solid + liquid) where the solid–liquid interface is explicitly tracked using marker points. The concentration and momentum equations are solved in the liquid region using an adaptive mesh of triangular elements that conforms to the interface. The velocity boundary conditions are applied directly on the interface. The model is validated using a series of problems that have analytical, experimental and numerical results. Four simulations are presented: (1) crystal growth of succinonitrile with thermal convection under two small undercoolings; (2) dendritic growth into an undercooled pure melt with a uniform forced flow; (3) equiaxial dendritic growth of a pure substance and an alloy with contraction-induced convection; and (4) directional solidification of Pb–0.2 wt% Sb alloy with convection driven by the combined action of contraction, thermal and solutal buoyancy. Some of the simulation results are compared to those reported using other methods including the phase-field method; others are new. In each case, the effects of convection on dendritic solidification are analysed. Copyright © 2005 John Wiley & Sons, Ltd.

KEY WORDS: dendritic solidification; moving boundary; convection; finite element; interface tracking; adaptive meshing

*Correspondence to: P. Zhao, Department of Mechanical Engineering, The University of New Mexico, Albuquerque, NM 87131, U.S.A.
†E-mail: pzhao@unm.edu
‡E-mail: heinrich@unm.edu
§E-mail: poirierd@u.arizona.edu

Contract/grant sponsor: National Aeronautics and Space Administration; contract/grant number: NCC8-96
Contract/grant sponsor: National Science Foundation; contract/grant number: DMR 0072955

Received 24 March 2005
Revised 24 March 2005
Accepted 30 March 2005

1. INTRODUCTION

It is well known that convection due to melt flow in solidification is unavoidable, and the effects of convection on the micro/macro-structures and various properties of the solidified metals and alloys can be significant [1–3]. Melt flow in solidification can be categorized into natural (or free) and forced convection. Included as natural convection is convection caused by contraction (or expansion) when the densities of the solid and liquid are different regardless of the presence of the gravitational force. Forced convection is induced by electromagnetic stirring, rotation, pouring of the melt, etc., some of which may be intentionally introduced to cause convection to enhance solute transport from the solid–liquid interface in order to reduce macro- and micro-segregations [1]. Natural convection is believed to be responsible for the discrepancies between experimental data under terrestrial conditions and the prediction of diffusion-based theories that ignore convection [3–6].

Numerical modelling of dendritic solidification without convection at the microstructural level has been extensively studied, and simulations have been performed in the last two decades using techniques such as the phase-field method, the level-set method and various explicit-interface-tracking methods. The extension of these methods to include convection in the melt, however, is much more recent starting only a few years ago. Most simulations of dendritic solidification with convection performed so far are for pure substances with forced flow. Tönhardt and Amberg [7, 8] used a phase-field method to simulate two-dimensional dendritic growth into an undercooled liquid subject to an externally forced flow. Their results show that the evolution of the dendrite shape was altered by the flow, and the growth of the side branches was promoted on the upstream side and inhibited on the downstream side as expected. Similarly, Beckermann *et al.* [9] and Tong *et al.* [10] studied the effects of a uniform-incoming flow on the operating point of the dendrite tip and the dynamics of dendritic side branching using a phase-field method. Al-Rawahi and Tryggvason [11] and Udaykumar *et al.* [12] presented simulations of dendritic solidification with forced flow using explicit front-tracking methods. Three dimensional simulations were reported by Jeong *et al.* [13, 14], Boettinger *et al.* [15] and Al-Rawahi and Tryggvason [16]. In all these simulations equiaxial growth was considered, in which the dendrite grows into an undercooled pure melt. Recently, Lan and Shih [17] presented simulation of dendritic growth into a supercooled binary melt subject to a forced flow using a phase-field method with an isothermal assumption. An 'antisolutal' trapping scheme was used to help relax the limitation on the interface thickness. Their simulations showed similar effects of an externally forced flow on a binary dendrite as on a thermal dendrite when both grow into an undercooled melt.

Simulations of dendritic growth with natural convection are few. Bänsch and Schmidt [18] presented a finite element model based on a sharp interface to simulate the effect of thermal convection on dendritic crystal growth in two space dimensions with either Dirichlet or absorbing boundary conditions for the flow problem, and Dirichlet or Neumann boundary conditions for the temperature. They obtained results for equiaxial solidification that showed strong influence of convection on dendritic morphology, side branching and growth rate. Tönhardt and Amberg [6] used the properties of succinonitrile to study the effects of thermal natural convection on crystal growth with a phase-field method coupled with Navier–Stokes equations. By comparing the results with and without convection for five different undercoolings ranging from 1.92 to 0.12 K, it was shown that the influence of thermal convection increases as the undercooling decreases, which confirms the experimental observations and theoretical

analyses that, at low undercoolings the effect of thermal convection becomes important [19]. For the larger undercoolings the influence of thermal convection is small or negligible.

Coriell *et al.* [20] considered the effect of flow due to a density change in eutectic growth of Sn–Pb and Fe–C alloys by extending the model of Jackson and Hunt [21] to allow for different densities of the melt and the phases within the solidified eutectic. They solved the decoupled steady-state momentum equations (analytically) and the solutal concentration equation (numerically), assuming a planar interface and Stokesian flow, to examine the effect of fluid flow on the relation between the interface undercooling, the structure spacing and the solidification rate. Conti [22] used a modified version of the phase-field method to simulate the growth of a free dendrite into a supercooled pure liquid subject to flow arising from the difference in the densities of the solid and liquid.

Even though dendritic solidification has been numerically studied for over two decades, a full numerical simulation for nondilute metallic alloys with properties found in real castings still remains challenging even in the absence of convection. The difficulties lie in the widely different length and time scales in the coupled energy and mass transport processes, the segregation of the solute upon solidification and the strong dependence of the melting temperature on the liquidus concentration [23, 24]. When convection is included, the problem is further complicated by the coupling of Navier–Stokes equations in the presence of evolving solid–liquid interfaces that need to be tracked as part of the solution.

Numerical simulation of flow with complex moving boundaries/interfaces[¶] constitutes a big challenge in CFD, even though it has been extensively studied for decades because of its importance in areas such as multiphase processes, flow–structure interactions, flow control, and bio-fluid mechanics. The challenge lies in the difficulty to accurately impose the boundary conditions at the exact location of the moving interface, which in general represents a discontinuity in both material properties and physical quantities.

Numerical methods to solve fluid flow equations with moving boundaries can be broadly divided into two categories based on the type of mesh used: the fixed Cartesian-grid methods and the adaptive mesh methods. Some of the methods that have only been applied to stationary boundaries but are claimed to be applicable to moving boundaries are also included in the following discussion. The first category can be further divided into the diffuse-interface methods, where the moving boundary is treated as an interface with a finite thickness of usually a few grid spacings, and the boundary conditions are approximated and spread over across the interface thickness, and the sharp interface methods, where the boundary conditions are applied somewhat directly at the interface. The diffuse-interface methods include the popular immersed boundary methods in CFD, where the effect of the immersed boundary on the fluid is approximated by a distribution of added singular sources (forces or vorticity) to the nearby grid points [9, 10, 25–28], and others that make use of a phase-field variable or similar function rather than adding a forcing term to the momentum equations [11].[||] The fixed-grid sharp interface methods include those that treat the interface as sharp both in the tracking and

[¶]The terms ‘boundary’ and ‘interface’ are used interchangeably throughout this paper unless otherwise indicated.

[||]References [6–8] would have been included here if the mesh used were fixed. In these references the no-slip condition at the evolving solidification front is realized by directly relating the flow field to the phase-field variable without adding an extra forcing term to the momentum equations. To get high resolution near the front while keeping the total number of elements minimal, an adaptive mesh was used.

in the imposition of the boundary conditions [29, 30]. An excellent discussion and a literature review on the fixed Cartesian-grid methods can be found in Reference [30].

The adaptive mesh methods include those that involve a changing mesh in the numerical procedure. The changing mesh may or may not conform to the moving interface. This category includes: (1) domain transformation (conformal mapping) and algebraic interpolation methods suitable for simple interface geometries and motion [31–34]; (2) node/mesh-moving methods that adjust the position of the nodes while preserving the mesh structure [35]; (3) remeshing methods that completely regenerate the mesh as the interface position changes [23]; and (4) methods that combine the remeshing and node-adjustment strategies [36]. In these methods, the mesh is always conformal to the interface. Other methods in this category use an adaptive mesh that is not body-conformal but is locally refined and regenerated as needed [6–8, 13, 14, 37], or they start with a coarse mesh and implement adaptive mesh refinement (AMR), which iteratively refines the elements in the region of large gradients in the solution [38, 39].

With finite-difference discretizations a Cartesian-grid method is often used in order to avoid the difficulties related to adapting the grid to the moving boundary and interpolation between the grids. In such a method the Navier–Stokes equations are solved on the fixed, usually uniform, grid that covers the whole domain consisting of both phases. The solid phase is modelled as a liquid with viscosity much higher than that of the liquid in the system. The Cartesian-grid methods are popular because of the simplicity of discretization and efficiency of the solver. These methods, however, have two drawbacks [40]. (1) It is difficult to use a locally refined grid in areas of interest, usually the vicinity of the interface, unless a fine grid is used for the whole domain, which is computationally prohibitive. Even though it is possible to use a fixed non-uniform grid, this technique becomes inefficient when the time-dependent interface is unknown and a large region of refined grid is needed to cover the possible positions of the interface resulting in large unwanted regions of refined grid. (2) It is difficult to accurately apply the interface conditions at the exact position on the immersed boundary, which is not aligned with the grid lines. In the generalized immersed boundary method [26], the forcing term is iteratively calculated and interpolated to the grid nodes by a feedback scheme until the flow velocity is brought back to the boundary velocity. Furthermore, the accuracy of the method is affected by the interpolation of the forcing term, which is defined on the interface, to the nearby grid points [27].

A finite volume method was used in the Cartesian-grid method presented by Udaykumar *et al.* [30], in which the interface conditions are realized by computing the momentum transport in control volumes formed in the cells traversed by the immersed boundaries. The method needs to deal with the so-called 'freshly cleared cells' problem, which lowers the accuracy of the method [41].

Adaptive body-conformal-mesh methods solve the momentum equations on a changing mesh that only covers the liquid region. The adaptive mesh can be easily refined near the immersed boundary or other areas of interest, and the exact boundary conditions at the moving interface can be applied at the correct position. The tradeoffs are the need to regenerate the mesh every time step (or every few time steps) and the interpolation required between the old and new meshes. All the difficulties encountered by a fixed-grid method are now transferred to finding an efficient way to generate a quality mesh conforming to the moving boundary. For simple geometries, the traditional domain transformation method is suitable as well as methods that involve moving the nodes or adjusting the elements while preserving the existing mesh

structure. A more systematic approach to generate body-fitted meshes resorts to the solution of partial differential equations, but this is computationally expensive for moving boundary problems. For complex geometries, direct numerical mesh generation is used.

In this article, we present a sharp-interface finite element model to simulate two-dimensional dendritic solidification of binary alloys with convection. This work is an extension of the model for dendritic solidification of binary alloys without convection presented in Reference [23], in which an interface conforming mesh was used to model the solute concentration equation in the liquid phase only. The same approach is used here based on the following considerations. (1) In dendritic solidification it is at the interface where the important physical processes take place. An adaptive mesh can be made very fine at the interface to accurately capture the interface dynamics and very coarse elements may be used to away from the interface where not much happens. (2) The same adaptive mesh constructed to solve the solute concentration equation can also be used for the solution of Navier–Stokes equations. The model is a sharp-interface model in that the solid–liquid interface is explicitly tracked, and the interfacial conditions for the energy, the solute concentration and the momentum equations are directly applied at the interface. The interface-tracking method is the same as originally presented in Reference [42]. The energy equation is solved on a fixed mesh of bilinear/triangular elements over the whole domain consisting of the solid and liquid phases. The solutal concentration and Navier–Stokes equations are solved on an adaptive mesh of triangular elements that covers only the liquid phase, using quadratic finite elements for the solutal concentration and linear finite elements for the velocity components. Details about the choice of meshes and elements and the coupling of different meshes are given in Section 3. The fractional-step method is used for the solution of Navier–Stokes equations for incompressible laminar flow, and the boundary conditions are directly applied at the interface.

There are two aspects of the present method that require special attention. One is the computational cost associated with the generation of the interface conforming mesh and the interpolation between two different meshes. An efficient adaptive mesh generator with a cost (for both mesh generation and interpolation) proportional to $N \log N$, where N is the total number of nodes, has been implemented [43–45], and this remeshing is done only in a subdomain slightly larger than the region within which the interface moves. The subdomain is a small fraction of the whole computational domain; in the rest of the domain the mesh is kept fixed. The second issue is the complexity of the moving interface that the mesh generator can handle. This has been addressed in References [23, 46], where it was shown that the two-dimensional mesh generator is very robust and can generate high-quality triangular-element mesh conforming to very complex interfaces.

All types of convection, including that generated by contraction, thermal and solutal buoyancy, and forced convection are included in this model. The material can be a pure substance or a binary alloy. By using graded variable meshes that are very fine near the interface and very coarse in the region far away from the interface, simulations can be performed in a domain several orders of magnitude larger than the size of the dendrites.

The simulations are validated against theoretical and experimental data and other published numerical results on three problems: the Rayleigh Bénard thermal convection problem, flow past a circular cylinder, and flow caused by an oscillating cylinder. Simulations of dendritic solidification including convection are validated using the work of Tönhardt and Amberg [6] for growth of succinonitrile crystals with natural thermal convection and very small undercoolings, and the simulation presented in References [9, 11] for dendritic growth

in the presence of forced convection. The effects of convection caused by contraction and thermosolutal buoyancy on the shape and growth rate of alloy dendrites are also examined.

In Section 2 the mathematical formulation of the problem is introduced, followed by the numerical implementation in Section 3. Simulation results and discussions are presented in Section 4. The last section contains some conclusions. Validation of the Navier–Stokes solver is given in the Appendix.

2. MATHEMATICAL FORMULATION

2.1. Governing equations

Consider a two-dimensional rectangular domain that contains the solid and liquid of a pure substance or binary alloy, Figure 1. The two phases are separated by a sharp interface which evolves during solidification. For equiaxial growth, the solid phase (initially a seed) is within the domain, Figure 1(a). In directional solidification under a temperature gradient, the solid phase initiates at the cooling side of the domain and evolves toward the other side, Figure 1(b). It is assumed that the liquid is incompressible, and the physical properties of the material are constant but different in each phase except for the density of liquid in the buoyancy term, in which the Boussinesq approximation is used. The dimensional forms of the governing equations for the temperature (T), the solute concentration (C), and the velocity and pressure ($\mathbf{u}, p$) are given by

$$\rho_{\mathrm{S}} c_{P\mathrm{S}} \frac{\partial T}{\partial t} = \nabla \cdot (\kappa_{\mathrm{S}} \nabla T) \tag{1}$$

$$\rho_{\mathrm{L0}} c_{P\mathrm{L}} \left(\frac{\partial T}{\partial t} + \mathbf{u} \cdot \nabla T \right) = \nabla \cdot (\kappa_{\mathrm{L}} \nabla T) \tag{2}$$

$$\frac{\partial C}{\partial t} + \mathbf{u} \cdot \nabla C = D_{\mathrm{L}} \nabla^2 C \tag{3}$$

$$\nabla \cdot \mathbf{u} = 0 \tag{4}$$

$$\frac{\partial \mathbf{u}}{\partial t} + \mathbf{u} \cdot \nabla \mathbf{u} = -\frac{1}{\rho_{\mathrm{L0}}} \nabla p + \nu \nabla^2 \mathbf{u} + \frac{\rho_{\mathrm{L}} - \rho_{\mathrm{L0}}}{\rho_{\mathrm{L0}}} \mathbf{g} \tag{5}$$

The energy equations (1) and (2) are written for the solid and liquid, respectively. The solute concentration and the velocity equations (3)–(5) are written in the liquid only. Solutal diffusion in the solid is ignored since the mass diffusivity in the solid is several orders of magnitude smaller than that in the liquid. The properties, $\rho, c_P, \kappa, D, \nu$ are density, specific heat, thermal conductivity, solutal diffusivity and kinematic viscosity, respectively, and $\mathbf{g}$ denotes the gravity vector. The subscripts S and L denote the solid and liquid phases, respectively. The density of the liquid in the body-force term of Equation (5) is assumed to be linear in T and C:

$$\rho_{\mathrm{L}} = \rho_{\mathrm{L0}}[1 - \beta_T (T - T_0) - \beta_C (C - C_0)] \tag{6}$$

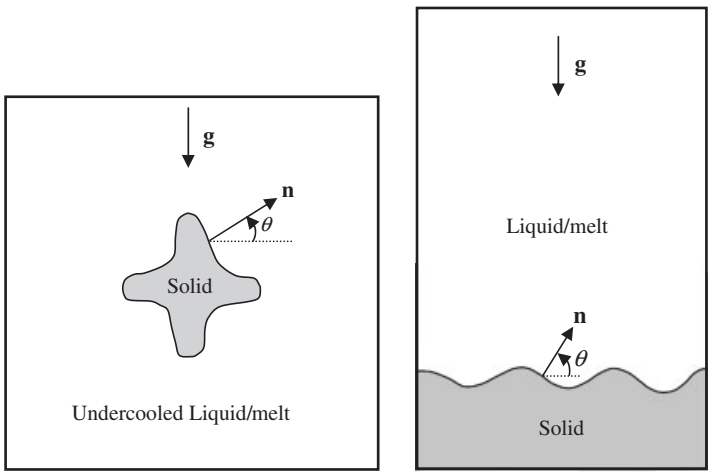

Figure 1. Computational domains: (a) equiaxial solidification driven by undercooling; (b) directional solidification driven by extracting heat from one side (the cooling side). **n** is the vector normal to the interface with an orientation denoted by θ and **g** denotes the gravity vector.

where $\beta_T \equiv -(1/\rho_{L0})\partial\rho_L/\partial T$ and $\beta_C \equiv -(1/\rho_{L0})\partial\rho_L/\partial C$ are the thermal and solutal expansion coefficients, respectively, ρ_{L0} is the liquid density at the base state, i.e. when $T = T_0$ and $C = C_0$, where C_0 is the initial bulk solutal concentration and T_0 is the liquidus temperature of the alloy when $C = C_0$. The conditions at the solid–liquid interface are the following:

$$T_S = T_L = T_I \tag{7}$$

$$(\kappa_S \nabla T_S - \kappa_L \nabla T_L) \cdot \mathbf{n} = \rho_S[L - (c_{PL} - c_{PS})(T_m - T_I)]V_I \tag{8}$$

$$-D_L \cdot \mathbf{n}\nabla C = (1 - k)(1 + \beta_S)CV_I \tag{9}$$

Conditions for the velocity and pressure are problem dependent and are described later. Here, T_I is the interface temperature, L is the latent heat assumed to be constant, $V_I \equiv (\mathrm{d}\mathbf{x}_I/\mathrm{d}t) \cdot \mathbf{n}$ is the growth velocity with $\mathbf{x}_I$ being the interface position vector, $\mathbf{n}$ is the unit vector normal to the interface, k is the equilibrium partition ratio, and β_S is the solidification contraction rate defined as $\beta_S = (\rho_S - \rho_{L0})/\rho_{L0}$. The interface temperature, T_I, is given by the generalized Gibbs–Thompson equation [47]

$$T_I - T_m + \frac{\gamma(\theta)T_m}{\rho_S L}\mathbb{C} + \frac{V_I}{\upsilon(\theta)} + \frac{T_m(c_{PL} - c_{PS})}{L}\left[T_I \ln\left(\frac{T_I}{T_m}\right) + T_m - T_I\right] = 0 \tag{10}$$

Here, $\gamma(\theta)$ and $\upsilon(\theta)$ are the anisotropic interfacial energy and kinetic mobility, respectively, and θ is the local interface orientation shown in Figure 1; $\mathbb{C}$ is the local interface curvature. For alloys the freezing temperature is related to the solute concentration through the phase diagram

of the material. For hypoeutectic lead–antimony (Pb–Sb) alloys, T_m can be approximated as

$$T_m = T_0 + m(C - C_0) \tag{11}$$

where m is the slope of the liquidus line. The initial and boundary conditions are problem dependent and are described for the individual cases in Section 4.

2.2. Nondimensionalization

A wide variety of situations, which have very different length and time scales, are considered. Hence, we use different sets of reference quantities for the nondimensionalization of the equations.

2.2.1. Directional solidification of a binary alloy with thermosolutal convection. For this type of problems, the reference quantities are: length H (to be defined in the individual cases), time H^2/D_L, velocity $\sqrt{gH\beta_C\Delta C}$, and pressure $\rho_{\mathrm{L}0}(D_\mathrm{L}/H)^2$. The temperature and concentration are made dimensionless by $(T - T_0)/\Delta T$ and $(C - C_0)/\Delta C$, respectively. The nondimensional governing equations are

$$\Lambda_p \frac{\partial T}{\partial t} = Le\nabla \cdot (\Lambda_K \nabla T) \tag{12}$$

$$\frac{\partial T}{\partial t} + \sqrt{R_C Sc}\mathbf{u} \cdot \nabla T = Le\nabla \cdot (\nabla T) \tag{13}$$

$$\frac{\partial C}{\partial t} + \sqrt{R_C Sc}\mathbf{u} \cdot \nabla C = \nabla^2 C \tag{14}$$

$$\nabla \cdot \mathbf{u} = 0 \tag{15}$$

$$\frac{\partial \mathbf{u}}{\partial t} + \sqrt{R_C Sc}\mathbf{u} \cdot \nabla \mathbf{u} = -\frac{1}{\sqrt{R_C Sc}}\nabla p + Sc\nabla^2 \mathbf{u} - \left(R_T Le\sqrt{\frac{Sc}{R_C}}T + \sqrt{R_C Sc}C\right)\mathbf{n}_\mathrm{g} \tag{16}$$

Here, $\Delta T = GL_\mathrm{S}$ with G the initial thermal gradient and L_S the length of the domain in the solidification direction, $\Delta C = C_0(1-k)/k$, $R_T = gH^3\beta_T\Delta T/\nu\alpha_\mathrm{L}$ the thermal Rayleigh number, $R_C = gH^3\beta_C\Delta C/\nu D_\mathrm{L}$ the solutal Rayleigh number, $Le = \alpha_\mathrm{L}/D_\mathrm{L}$ the Lewis number, $Sc = \nu/D_\mathrm{L}$ the Schmidt number, $\Lambda_P = \rho_\mathrm{S}c_{P\mathrm{S}}/\rho_{\mathrm{L}0}c_{P\mathrm{L}}$, $\Lambda_K = \kappa_\mathrm{S}/\kappa_\mathrm{L}$, and $\mathbf{n}_\mathrm{g}$ is the unit vector in the direction of gravity. The nondimensional interfacial conditions are

$$T_\mathrm{S} = T_\mathrm{L} = T_\mathrm{I} \tag{17}$$

$$T_\mathrm{I} - T_m + (1 + \beta_m C)\sigma\mathbb{C} + \mu V_\mathrm{I} + \beta_c St(T_\mathrm{I} - T_m)^2 = 0 \tag{18}$$

$$Le(\Lambda_K \nabla T_\mathrm{S} - \nabla T_\mathrm{L}) \cdot \mathbf{n} = (1 + \beta_\mathrm{S})(1/St + \beta_c(T_\mathrm{I} - T_m))\sqrt{R_C Sc}V_\mathrm{I} \tag{19}$$

$$-\nabla C \cdot \mathbf{n} = (1 + \beta_\mathrm{S})\sqrt{R_C Sc}(k + (1-k)C)V_\mathrm{I} \tag{20}$$

where the dimensionless parameters are: $\beta_m = mC_0/T_0$, $\beta_c = (c_{P\mathrm{L}} - c_{P\mathrm{S}})/c_{P\mathrm{L}}$ the differential specific heat, $St = c_{P\mathrm{L}}\Delta T/L$ the Stefan number, $\sigma = \sigma_0 f(\theta)$ the interfacial energy with

$\sigma_0 = \gamma_0 T_{m0}/\rho_S LH\Delta T$ and $\mu = \mu_0 g(\theta)$ the kinetic mobility with $\mu_0 = \sqrt{gH\beta_C \Delta C}/\upsilon_0 \Delta T$, γ_0 and υ_0 being the interface energy and kinetic mobility, respectively, at the reference state (i.e., $T = T_0$ and $C = C_0$), and $f(\theta)$ and $g(\theta)$ being the anisotropic functions for the interfacial energy and kinetic mobility, respectively. The derivation of Equation (18) from Equation (10) is given in Reference [23].

2.2.2. Solidification of a pure substance with thermal convection. For dendritic growth into an undercooled pure melt with thermal convection, the following reference quantities are chosen for nondimensionalization: length H, time H^2/α_L, velocity $\sqrt{gH\beta_T \Delta T}$, and pressure $\rho_{L0}(\alpha_L/H)^2$. The temperature is made dimensionless by $(T - T_m)/\Delta T$, where ΔT is the undercooling. The dimensionless governing equations are

$$\Lambda_p \frac{\partial T}{\partial t} = \nabla \cdot (\Lambda_K \nabla T) \tag{21}$$

$$\frac{\partial T}{\partial t} + \sqrt{R_T Pr}\mathbf{u} \cdot \nabla T = \nabla \cdot (\nabla T) \tag{22}$$

$$\nabla \cdot \mathbf{u} = 0 \tag{23}$$

$$\frac{\partial \mathbf{u}}{\partial t} + \sqrt{R_T Pr}\mathbf{u} \cdot \nabla \mathbf{u} = -\frac{1}{\sqrt{R_T Pr}} \nabla p + Pr \nabla^2 \mathbf{u} - \sqrt{R_T Pr} T \mathbf{n}_g \tag{24}$$

where $Pr = v/\alpha_L$ is the Prandtl number. The interfacial conditions are

$$T_S = T_L = T_I \tag{25}$$

$$T_I + \sigma \mathbb{C} + \mu V + \beta_c St T_I^2 = 0 \tag{26}$$

$$(\Lambda_K \nabla T_S - \nabla T_L) \cdot \mathbf{n} = (1 + \beta_S)(1/St + \beta_c (T_I - T_m))\sqrt{R_T Pr} V_I \tag{27}$$

2.2.3. Solidification of a pure substance with forced convection. For dendritic growth into an undercooled pure melt with forced convection only (natural convection due to contraction or thermal buoyancy is ignored), the following reference quantities are used for nondimensionalization: length H, time H^2/α_L, velocity U_∞, and pressure $\rho_{L0} U_\infty \alpha_L/H$. The temperature is made dimensionless by $(T - T_m)/\Delta T$, where ΔT is the undercooling. The dimensionless governing equations are

$$\Lambda_p \frac{\partial T}{\partial t} = \nabla \cdot (\Lambda_K \nabla T) \tag{28}$$

$$\frac{\partial T}{\partial t} + Pe_f \mathbf{u} \cdot \nabla T = \nabla \cdot (\nabla T) \tag{29}$$

$$\nabla \cdot \mathbf{u} = 0 \tag{30}$$

$$\frac{\partial \mathbf{u}}{\partial t} + Pe_f \mathbf{u} \cdot \nabla \mathbf{u} = -\nabla p + Pr \nabla^2 \mathbf{u} \tag{31}$$

where $Pe_f = U_\infty H/\alpha_L$ is the flow Peclet number. The corresponding interfacial conditions are

$$T_S = T_L = T_I \tag{32}$$

$$T_I + \sigma\mathbb{C} + \mu V + \beta_c St T_I^2 = 0 \tag{33}$$

$$(\Lambda_K \nabla T_S - \nabla T_L) \cdot \mathbf{n} = (1 + \beta_S)(1/St + \beta_c(T_I - T_m))Pe_f V_I \tag{34}$$

3. NUMERICAL METHOD AND PROCEDURE

3.1. Interface tracking and mesh generation

The solid–liquid interface is represented using marker points in a sequential order and tracked in the temperature mesh which is uniform and fixed and covers the whole domain. Details regarding the tracking scheme and the interaction between the moving interface and fixed-mesh elements have been presented in References [23, 24, 42] and are not repeated here. The adaptive mesh, on which the concentration and the momentum equations are solved, covers the liquid region only and is generated every time step using the current interface location as part of the domain boundary. The adaptive mesh consists of triangular elements, which are finest at the interface and become coarser away from the interface. Details regarding the efficiency of the generation of the adaptive mesh and the quality of the mesh are given in Reference [23].

3.2. Interpolation between meshes

The field quantities (T, C, u, v, p) are interpolated between the uniform mesh and the adaptive mesh and between two consecutive adaptive meshes. It was found in Reference [23] that quadratic triangular elements are needed for the interpolation of the solutal concentration in order to conserve mass in the solute boundary layer ahead of the solidification front, where the concentration changes dramatically. For the velocity and pressure, however, linear triangular elements are sufficient.

3.3. Discretization

The finite element method with a Petrov–Galerkin formulation is used to discretize the equations. The θ-method, which corresponds to the second-order-in-time Crank–Nicolson scheme, is used for the discretization in time. The convective terms are treated explicitly so that the final stiffness matrix is symmetric and positive-definite, and an iterative conjugate gradient solver with preconditioning is used to obtain the solution. The Navier–Stokes equations are solved using a fractional-step method. Depending on the mesh size and boundary conditions, the pressure is solved with a sparse direct solver or an iterative solver.

3.4. Solution procedure

1. At time t_n, the temperature, concentration, interface position and its velocity, the liquid velocity and pressure are all known.
2. A new interface position is obtained by moving each marker on the interface in the normal direction with its calculated velocity.

3. A mesh of triangular elements that conforms to the new interface and covers the liquid region is generated.
4. The solute concentration, liquid velocity and pressure at the last time step are interpolated from the old mesh to the new mesh. Liquid velocity is also interpolated from the old adaptive mesh to the fixed uniform mesh.
5. Using the current interface velocity and liquid velocity, the new temperature and solute concentration are solved.
6. The equilibrium freezing temperature at the interface is calculated from Equation (11), and the interface temperature T_I is then calculated from Equation (10).
7. A new interface velocity is calculated for each marker from Equation (8) and is compared with the previous velocity. If the relative difference at each marker is less than a prescribed tolerance, go to next step. Otherwise, a new interface velocity is obtained at each marker using the previous velocity and the newly calculated velocity combined using a relaxation parameter [42], and the program goes back to step 5.
8. The fluid velocity and the pressure are solved using the most recent temperature and concentration for the gravity term. The program goes back to step 1 for the next time step.

4. RESULTS OF SOLIDIFICATION WITH CONVECTION

4.1. Growth of succinonitrile crystals with thermal convection

Numerical simulation of the effect of thermal convection on the growth of succinonitrile (SN) crystals into an undercooled melt was done by Tönhardt and Amberg [6] who used a phase-field method. In order to compare the numerical results with experimental data, Tönhardt and Amberg used undercoolings from 1.92 to 0.12 K, which are within the range used in the experiments. The corresponding dimensionless undercooling $\Delta = c_p(T_m - T_\infty)/L (\Delta = -St)$ is between 0.08 and 0.005. With such small undercoolings, the thermal boundary layer at the interface is large. Hence, the computational domain must be very large compared to the size of the crystal in order to eliminate the boundary effects. The domain used in Tönhardt and Amberg [6] was four orders of magnitude larger than the size of the initial seed and two orders larger than the final grown crystal. To obtain good resolution at the interface in such a big domain, the only reasonable choice is to use an adaptive grid strategy to keep the computational expense within reasonable bounds.

In order to compare our numerical results to those reported in Reference [6], the same properties of SN as listed in Table I of Reference [6] and the same domain size are used. Because of symmetry, only half of the full square domain is used. The computational domain with the boundary conditions is shown in Figure 2. Equations (21)–(24) are solved with these boundary conditions and the interfacial conditions given by Equations (25)–(27). The dimensionless material parameters are $\Lambda_p = \Lambda_K = 1$, $\beta_c = \beta_S = 0$, $Pr = 23.2$, and $\mu_0 = 0$. The dimensionless anisotropic interfacial energy is

$$\sigma = \sigma_0(1 - 15\varepsilon \cos 4\theta), \quad \varepsilon = 0.015 \tag{35}$$

where $\sigma_0 = \gamma_0 T_m/\rho_S LH\Delta T$. The Rayleigh number $R_T(= gH^3\beta_T\Delta T/\alpha_L v)$ and σ_0 are dependent of the length scale H and the undercooling ΔT. The length scale H is a multiple of the capillary length, $d_0 = \gamma_0 c_p T_m/L^2 = 2.568 \times 10^{-6}$ mm.

Table I. Simulation parameters that depend on the undercooling.

Δ	ΔT (K)	H (mm)	σ_0	R_T
0.04	0.96	1.284×10^{-3}	5.00×10^{-2}	5.54×10^{-8}
0.02	0.48	2.568×10^{-3}	5.00×10^{-2}	2.22×10^{-7}

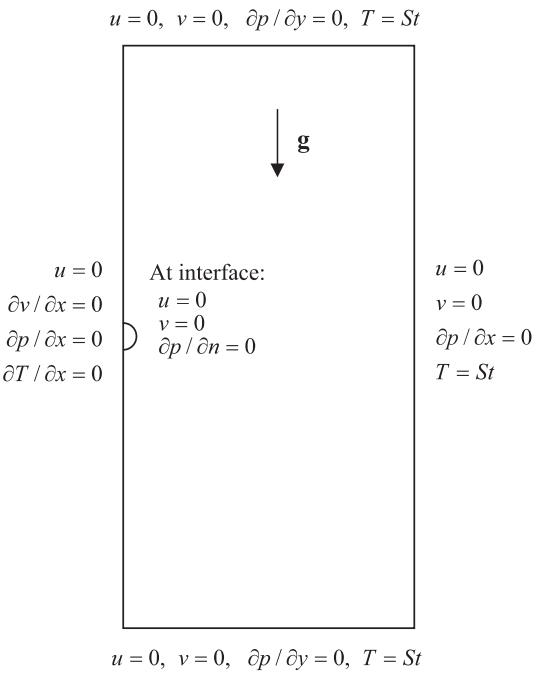

Figure 2. Computational domain with boundary conditions for crystal growth of succinonitrile with thermal convection. The half-circle represents the initial seed.

Simulations were performed for two values of the dimensionless undercooling Δ, 0.04 and 0.02, for which the length scale H is $500d_0$ and $1000d_0$, respectively. The dimensional undercooling $\Delta T = T_m - T_\infty$, the length scale H, the interfacial energy coefficient σ_0 and the Rayleigh number R_T are listed in Table I. The flow field for $\Delta = 0.02$ at dimensionless time of 1.64×10^6 is shown in Figure 3, which compares to Figure 2 of Tönhardt and Amberg [6]. Figure 3(a) shows the flow vector in the full domain. The crystal is so small compared to the full domain that it appears as a dot within a small box indicated by dotted lines in the centre of the domain. The flow caused by thermal buoyancy due to latent heat release on the crystal surface forms two vortices above the crystal. The vortices are being freely driven up by the thermal buoyancy; the centre of the vortices at this simulation time has just passed the height 20×10^3. The boundary effects on the vortices at this time point are still minimal due to the large computational domain used. It can been seen that the strongest convection occurs right above the crystal between the two vortices; the maximum flow velocity is 0.056, about

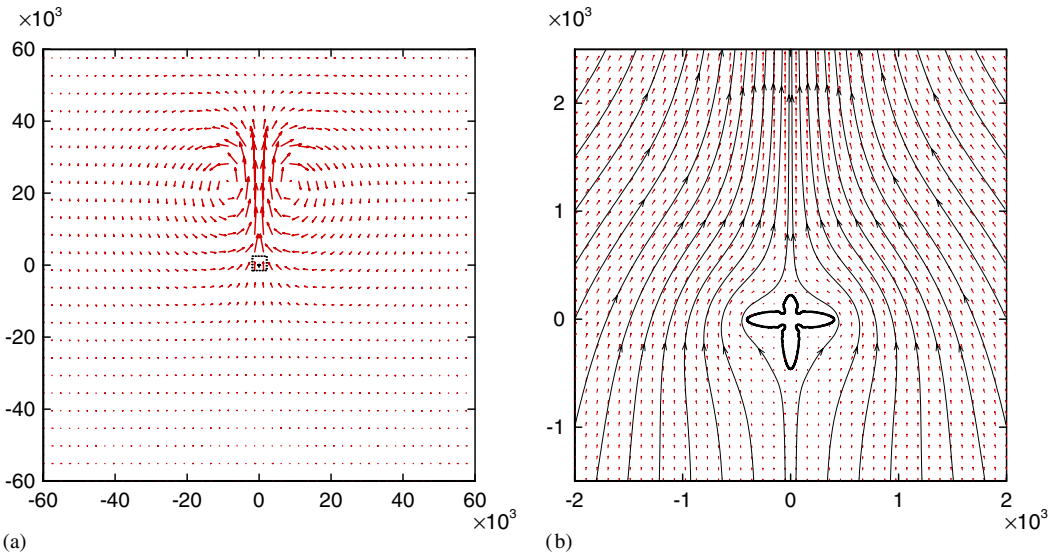

Figure 3. Flow velocity vector in crystal growth of succinonitrile with thermal convection: (a) full domain; and (b) local flow vector around the crystal. The region plotted is indicated in (a) with dotted lines.

200 times larger than the tip growth velocity (2.82×10^{-4}) of the downward growing crystal arm. The flow around the crystal within the small box indicated in Figure 3(a) is shown in Figure 3(b). The temperature contours corresponding to Figure 3 are shown in Figure 4, which is plotted in a similar way as Figure 3 in Reference [6]. While the values of these contours are not given in Reference [6], the shapes of temperature contours look almost identical in the two figures.

The solid–liquid interfaces with and without convection are shown in Figures 5(a) and 5(b) for $\Delta = 0.04$ and $\Delta = 0.02$ at times 1.28×10^6 and 1.64×10^6, respectively, which compare and agree well to Figures 4(a) and 4(b) of Reference [6], respectively. The difference in the size of the dendrites between the convective and nonconvective cases is larger for $\Delta = 0.02$ than $\Delta = 0.04$, indicating the effects of thermal convection on the dendrite growth is stronger as the undercooling decreases. Also the horizontally growing dendrite arms for the smaller undercooling are bent slightly downward because of the convection.

The tip velocities versus time for the downward, horizontal and upward growing dendrite arms are plotted in Figure 6. While the growth of the downward growing dendrite arm reaches quasi-steady state at approximately 1.0×10^6 and 1.3×10^6 for $\Delta = 0.04$ and $\Delta = 0.02$, respectively, the tip velocity of the upward growing dendrite arm keeps decreasing all the time. The time history of the growth of the horizontal dendrite arms is similar to that of the one growing downward except at a lower growth rate: the tip velocity rapidly drops to a minimum value in the initial transient stage and then slightly increases and reaches a steady state. The tip velocity and radius of the downward growing dendrite arm at the end of the simulation are listed in Table II together with Tönhardt and Amberg's results.

The fixed mesh used for the temperature in the case of $\Delta = 0.02$ has close to 290 000 elements, about half of which are uniform square elements covering the dendritic growth

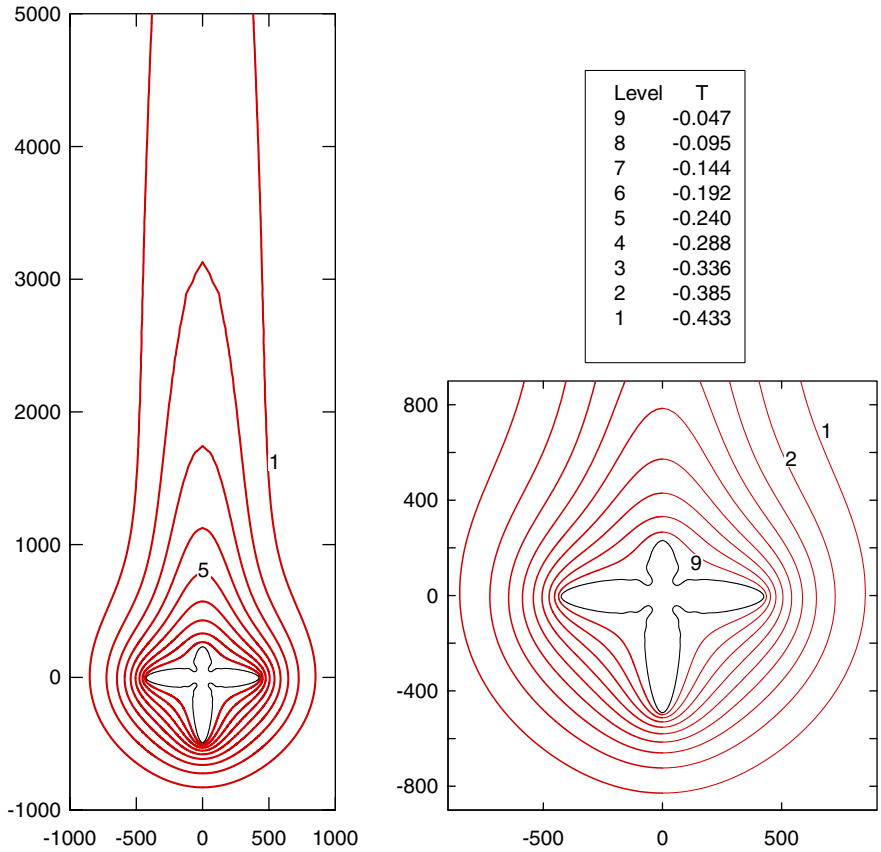

Figure 4. Isotherms around the dendrite showing the effects of convection: (a) the closed isotherms are stretched up by the upward convection; and (b) close-up around the dendrite.

region (about 1% of the whole domain in single dimension or 0.01% in area). The remaining elements are unstructured triangles covering the remaining 99.99% of the domain. The adaptive mesh for the momentum equations consists of all triangular elements, whose number varies with the arc length of the interface: approximately 173 000 and 276 000 elements at the beginning and end of the simulation, respectively. The CPU time for this case is approximately 114 hours on a HP/Compaq Alpha GS1280 machine (one processor), about a quarter of which is spent to solve for the temperature, a quarter for the momentum equations and the rest for the remeshing and interpolation.

4.2. Forced convection

Dendritic growth into an undercooled pure melt with an imposed uniform-incoming flow has been numerically simulated by several authors [9, 11, 12]. Here we consider the same case that was simulated by Beckermann *et al.* [9] and Al-Rawahi and Tryggvason [11] in order

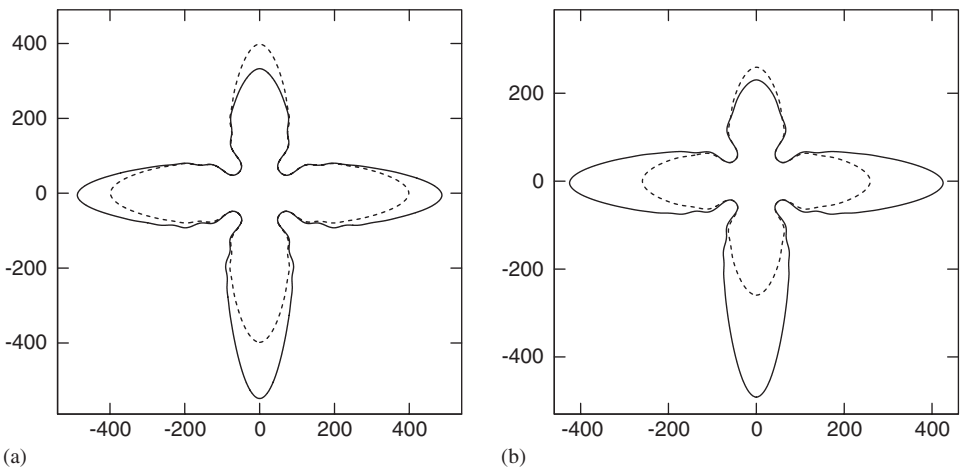

Figure 5. Comparison of the solid–liquid interface with and without convection: (a) $\Delta = 0.04$; and (b) $\Delta = 0.02$.

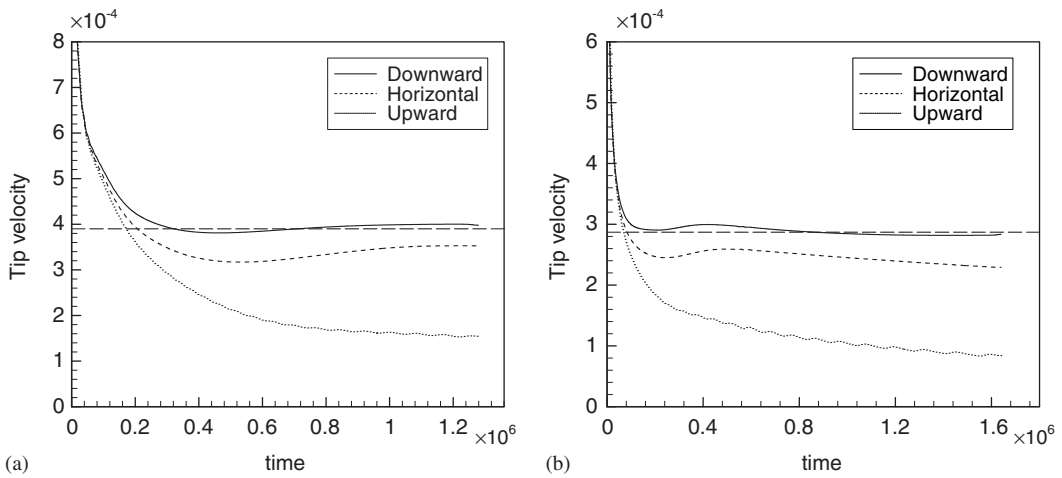

Figure 6. Tip velocity versus time for the downward, horizontally and upward growing dendrite arms: (a) $\Delta = 0.04$, (b) $\Delta = 0.02$. The horizontal dash-lines indicate the tip velocity of the downward growing dendrite arm at times 1.28×10^6 and 1.64×10^6 for $\Delta = 0.04$ and $\Delta = 0.02$, respectively, reported in Reference [6].

to compare our results with theirs. The computational domain and the boundary conditions for the velocity components, pressure and temperature are illustrated in Figure 7. Symmetry is imposed in the current simulation. The thermal properties of the solid and liquid are the same. Equations (28)–(31) are solved with interfacial conditions, Equations (32)–(34), and the boundary conditions given in Figure 7. The dimensionless material parameters are

Table II. Tip velocity (V_{tip}) and radius (R_{tip}) and arm length (L_{arm}) of the downward growing dendrite arm at the end of simulation.

	0.04			0.02		
Undercooling (Δ)	V_{tip}	R_{tip}	L_{arm}	V_{tip}	R_{tip}	L_{arm}
Tönhardt and Amberg [6]	3.9×10^{-4}	14.75	563	2.87×10^{-4}	12	500
Current results	3.98×10^{-4}	13.3	548	2.82×10^{-4}	11.1	491

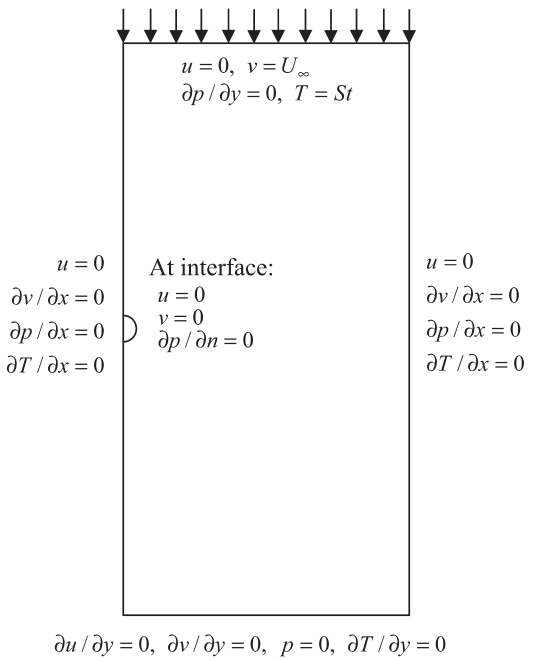

Figure 7. Computational domain and boundary conditions for dendritic growth with forced convection. Due to symmetry the computational domain is only half of the simulated physical domain. The half-circle represents the initial seed.

$\Lambda_p = \Lambda_K = 1$, $\beta_c = \beta_S = 0$, $Pr = 23.1$, and $\mu_0 = 0$. The interfacial energy anisotropy function is given by Equation (35) with $\varepsilon = 0.05$. The two controlling parameters are the Stefan number, St, and the flow Peclet Number, Pe_f, which take the values of -0.55 and 0.035, respectively.

Since the undercooling $St = -0.55$ is rather high, the computational domain need not be very large to exceed the thermal boundary-layer around the dendrite. The velocity boundary-layer, however, extends to approximately five times the thermal boundary layer. The current simulation uses a nondimensional domain of $5000 \times 10\,000$ based on the capillary length, which is about five times larger than the domain used by Al-Rawahi and Tryggvason [11] and three time larger than the largest domain used by Beckermann *et al.* [9]. The finite element mesh is non-uniform; the size of the finest elements is about 2.5 nondimensional units. A typical mesh for the momentum equations consists of 57 000 nodes and 114 000

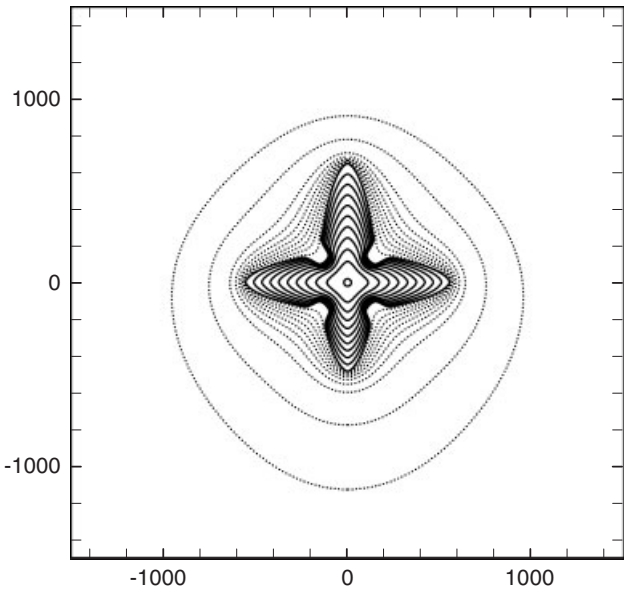

Figure 8. The temperature field and the interface at nondimensional time 2.5×10^4. The interface is shown at equal time intervals of 2.5×10^3.

triangular elements. The mesh for the energy equation contains close to 110 000 nodes and 140 000 mixed quadrilateral and triangular elements.

Figure 8 shows the dendrite and the temperature field at the nondimensional time of 2.5×10^4. The interface evolution is shown at equal time intervals of 2.5×10^3. The outer contour represents the thermal boundary layer defined as 99.99% of the undercooling, well contained within the computational domain. However, the velocity gradients extend to a much larger region as demonstrated in Figures 9(a) and 9(b), which show the contours of the velocity components. The time histories of the tip velocities of the upstream, the perpendicular and the downstream dendrite arms are plotted in Figure 10, which shows converged steady-state velocities of the tips. The tip velocity of the downstream arm decreases very slowly at the end of the simulation and has almost reach a steady state. The tip velocities and tip radii of the three dendrite arms at or near the steady state are listed in Table III together with the results reported in References [9, 11].

4.3. Convection induced by contraction

Most materials undergo contraction (or expansion) upon solidification because the densities of the liquid and solid phases are different. Obviously, contraction (expansion) upon solidification induces the melt to flow toward (away from) the solid–liquid interface, and the convection changes the temperature and solute concentration distribution ahead of the interface and thereby the evolution of the interface. Depending on the magnitude of the solidification contraction, contraction-induced convection can be stronger than buoyancy-induced convection

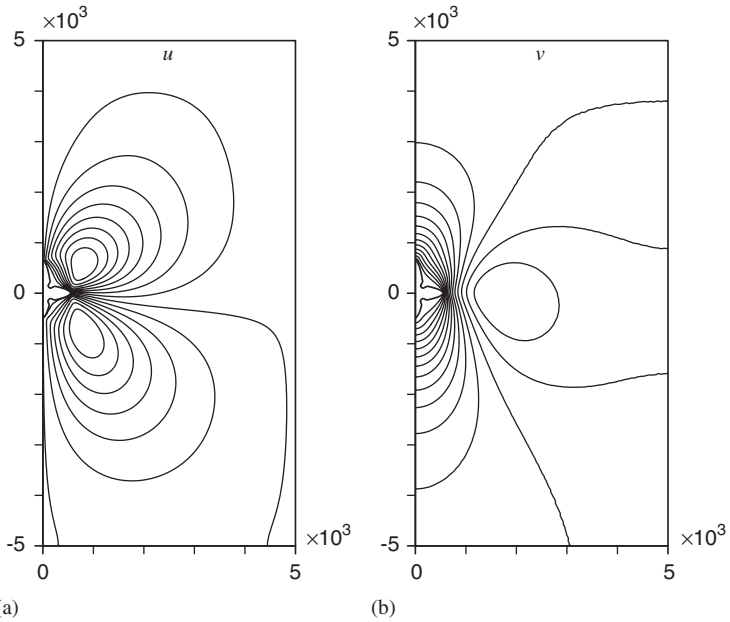

Figure 9. Contours of flow velocity components showing the region of velocity gradients: (a) u component; and (b) v component.

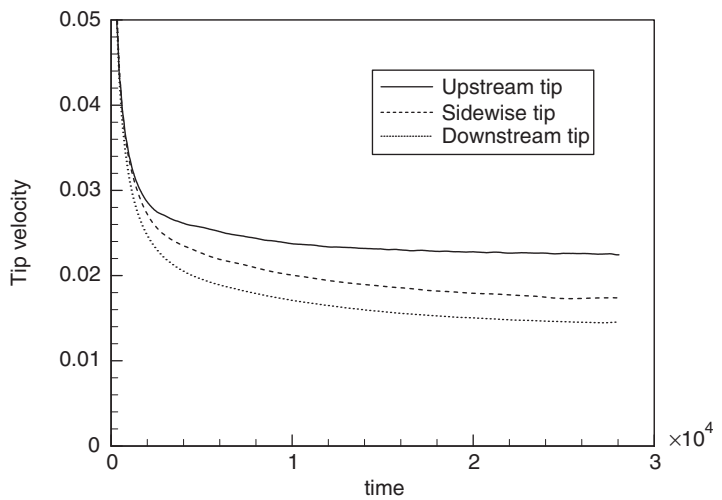

Figure 10. Time history of tip velocities of the upstream, sidewise and downstream dendrite arms.

and have significant effects on dendritic growth. With the exception of the work by Conti [22], however, contraction-induced convection has not been considered in previous simulations of dendritic growth.

Table III. Tip velocity (V_{tip}) and radius (R_{tip}) in the case of forced convection. $Pe_f = 0.035$, $St = -0.55$, $Pr = 23.1$, $\varepsilon = 0.05$ (NA – not available).

Dendrite arm tip	Upstream		Sidewise		Downstream	
Velocity, radius	V_{tip}	R_{tip}	V_{tip}	R_{tip}	V_{tip}	R_{tip}
Beckermann *et al.* [9]	0.0244	7.46	0.0174	6.9	0.0120	7.0
Al-Rawahi and Tryggvason [11]	0.0244	6.3	0.0170	7.4	NA	7.5
Current results	0.0225	6.1	0.0173	7.1	0.0145	7.2

By mass conservation, the flow velocity at the interface is related to the solidification contraction (β_S), the interface velocity (V_I) and the interface normal vector ($\mathbf{n}$) through the following relation:

$$\mathbf{u} = -\beta_S V_I \mathbf{n} \tag{36}$$

which is valid for both contraction and expansion (solidification and remelting). Since in our model the interface position, velocity and curvature are explicitly calculated and the mesh for the momentum equations conforms to the interface, it is straightforward to impose the interfacial velocity conditions at the exact position.

As a first example, equiaxial dendritic growth of a model pure substance into its undercooled melt is considered with convection induced by contraction alone. The nondimensional material properties are $\Lambda_p = \Lambda_K = 1$, $\beta_S = 0.1$, $Pr = 1$, $\beta_c = 1 - \Lambda_p/(\beta_S - 1)$ and $\sigma_0 = \mu_0 = 0.001$. The anisotropy function for the interfacial energy is similar to that used by Juric and Tryggvason [48],

$$f(\theta) = 1 + A_\sigma \left(\frac{8}{3} \sin^4 \left(\frac{1}{2} m_\sigma (\theta - \theta_\sigma) \right) - 1 \right) \tag{37}$$

with $A_\sigma = 0.4$, $m_\sigma = 6$ and $\theta_\sigma = 30°$, where m_σ specifies the mode of the symmetry of the dendrite. The dimensionless undercooling is $St = -0.8$. A seed is initially placed in the centre of the computational domain, which is a square of 4×4 units. The initial seed is a perturbed circle specified by $x = x_c + R\cos(\theta)$, $y = y_c + R\sin(\theta)$, where (x_c, y_c) is the centre of the domain and $R = R_0 + \varepsilon_s \cos(m_s(\theta - \theta_s))$ with $R_0 = 0.1$, $\varepsilon_s = 0.02$, $m_s = m_\sigma$, and $\theta_s = \theta_\sigma$. The perturbation in the seed is aligned with the symmetry mode of the interfacial energy anisotropy. The boundary conditions are $T = St$, $\mathbf{n} \cdot \nabla u = 0$, $\mathbf{n} \cdot \nabla v = 0$ and $p = 0$. All the boundaries of the domain are open so the melt is free to enter the domain to fill the mass deficit caused by solidification contraction.

The second example is similar to the first one except the material is an alloy. Besides the parameters given above, new parameters related to the species are needed; they are initial uniform concentration $C_0 = 2.2$, the segregation ratio $k = 0.4$, the slope of the liquidus $m = 0.035$ and the Lewis number $Le = 10$. The boundary condition for the solute concentration is $C = C_0$.

Figures 11(a)–11(d) show the interface evolution for the above two cases together with their counterparts without convection. The simulation times for all the four cases are the same and the interface is shown at equal intervals of 0.01. The convection caused by contraction enhances the growth rate and destabilizes the interface, and the growth of the dendrite is enhanced in all directions. This is expected since convection by contraction has similar

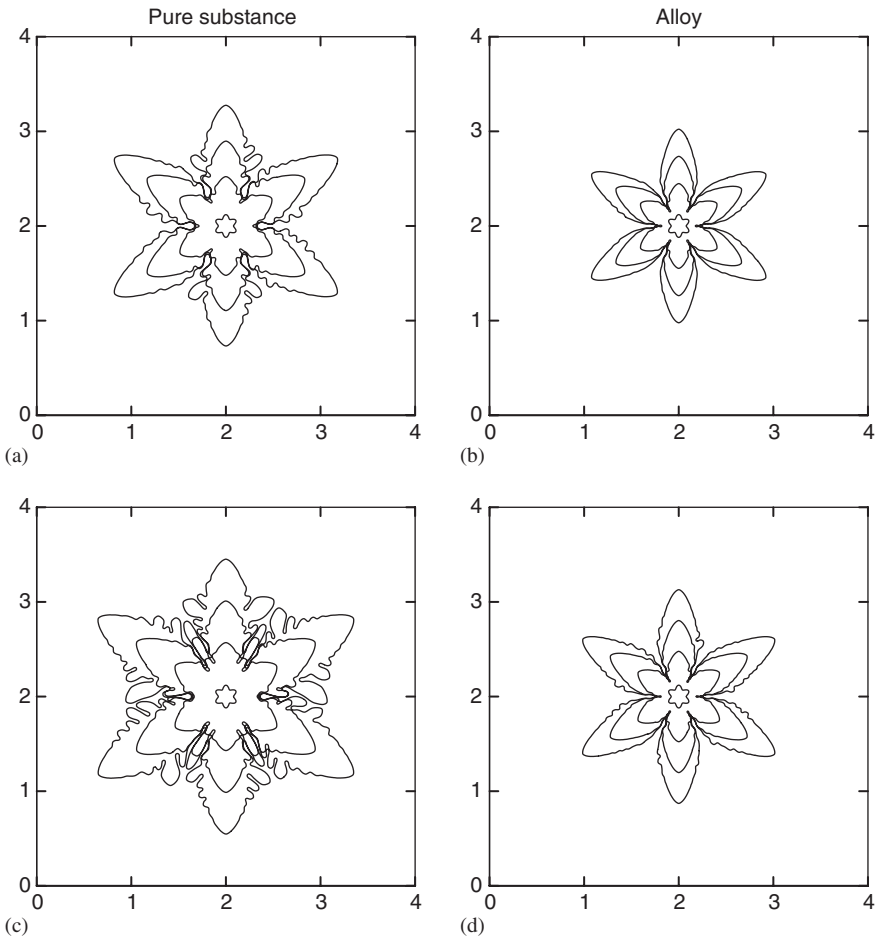

Figure 11. Comparison of interface morphology in equiaxial solidification of a pure substance and an alloy with and without contraction-induced convection: (a) pure substance without convection; (b) alloy without convection; (c) pure substance with convection; and (d) alloy with convection. The simulation times for the four cases are the same, and the interface is shown at equal intervals of 0.01.

effects on all dendrite arms (including secondary dendrite arms) as a forced flow has on an upstream-growing dendrite arm. The mutual enhancement between local solidification rate and convection destabilizes the interface as any protuberance causes stronger convection locally. It can also be seen from Figure 11 that the effects of convection on dendritic growth are more significant for the pure substance than for the alloy. That is because solidification is faster and convection is stronger in the pure substance case. The buildup of the solute concentration near the interface due to solute segregation upon solidification slows down the dendrite growth.

The velocities together with the dendrite outlines for the pure substance and the alloy are shown in Figure 12. As expected the flow velocity is maximal at the dendrite tips and some narrow openings of inter-dendritic regions and minimal in the grooves of the dendrite.

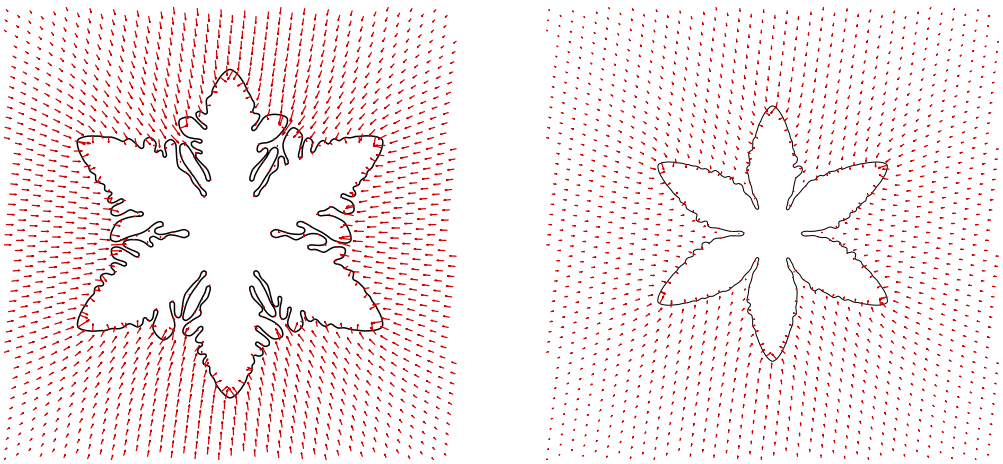

(a) (b)

Figure 12. Flow velocity vectors in equiaxial dendritic growth with contraction-induced convection: (a) pure substance; and (b) alloy. The dendrite outline is shown as the inner boundary of the flow field.

4.4. Directional solidification with mixed convection

Thermosolutal convection with and without contraction is considered for the directional solidification of Pb–0.2 wt% Sb alloy. The physical properties of the alloy are listed in Table IV. The problem setup is illustrated in Figure 1(b). The computational domain is a square of 0.8×0.8 mm, corresponding to a nondimensional domain of $(3.32 \times 10^5)^2$ based on the capillary length $d_0 = \gamma_0 c_{PL} T_{m0}/\rho_{L0} L^2$. Initially, the domain is all melt with a uniform concentration of $C_0 = 0.2$ wt% Sb and a thermal gradient $G = 1.008$ K/mm in the vertical direction. Solidification is initiated and subsequently driven by extracting heat at the cooling rate $C_R = 0.039$ K/s from the bottom (the cooling end) while maintaining the thermal gradient on the top. Based on $\Delta T = GH$ (H is set to be 1 mm) and $\Delta C = C_0(1-k)/k$, the interfacial energy and kinetic mobility coefficients are $\sigma_0 = 4.63 \times 10^{-5}$ and $\upsilon_0 = 0.618$. Equation (35) is used for the anisotropic interfacial energy with $\varepsilon = 0.0267$ and the kinetic mobility is constant (no anisotropy).

As solidification proceeds the plane-front breaks down and dendrites evolve. The solute concentration builds up at the roots of the dendrites; this tends to destabilize the system with respect to convection since the solute (Sb) is less dense than the solvent (Pb). On the contrary the temperature distribution stabilizes the system since the melt is cooler at the bottom and the thermal expansion is positive. The effect of the thermal gradient on the instability is much smaller than that of the concentration gradient; at the beginning of the simulation the thermal Rayleigh number is $R_T = 0.174$ based on the height of the melt region and the solute Rayleigh number is $R_C = 1643$ based on thickness of the solutal boundary layer where the concentration gradient exists. This thickness is defined as the distance from the interface to the position where the concentration dropped 99% in the boundary layer. According to linear stability theories [49], the critical Rayleigh number for the onset of convective instability is 1100 for one-rigid one-free boundary conditions which is a good approximation to the current problem set-up when there is no contraction.

Table IV. Physical properties of alloy Pb–0.2 wt% Sb.

Property	Symbol and unit	Value
Bulk concentration of Sb	C_0, wt%	0.2
Liquid density at base state	ρ_{L0}, kg/mm^3	1.042×10^{-5}
Solute diffusivity	D_L, mm^2/s	2.0×10^{-3}
Solute segregation ratio	k	0.4
Slope of liquidus line	m, K/wt%	-5.0
Melting temperature of pure solvent	T_{m0}, K	600.0
Latent heat of fusion	L, J/kg	29775
Heat conductivity in solid	κ_S, J/s mm K	0.023
Heat conductivity in liquid	κ_L, J/s mm K	0.023
Specific heat of solid	c_{PS}, J/mm^3 K	1.52×10^{-3}
Specific heat of liquid	c_{PL}, J/mm^3 K	1.52×10^{-3}
Thermal expansion coefficient	β_T, K^{-1}	1.22×10^{-4}
Solutal expansion coefficient	β_C, 1/wt%	5.88×10^{-3}
Solidification contraction	β_S	0.0532
Interfacial energy	γ_0, J/mm^2	2.54×10^{-8}
Kinetic mobility	υ_0, mm/s K	6.67
Lewis number	Le	7565
Prandtl number	Pr	0.0124
Schmidt number	Sc	93.8

Similar to the procedure used in Reference [23], to save computational time the one-dimensional model is run first, and the temperature and concentrations from the one-dimensional calculations are then used as initial conditions to start the full two-dimensional calculations. For a given combination of thermal gradient G and cooling rate C_R, there is a corresponding one-dimensional steady-state solution of the temperature and concentration. The thermal gradient and the cooling rate are chosen so that at the final one-dimensional steady state constitutional undercooling is established at the interface, and the perturbation of the planar interface grows in the following two-dimensional calculations. In this case a perturbation cosine wave with wavelength 0.1 mm and amplitude 0.0036 mm is applied to the interface position in the vertical direction. Symmetry boundary conditions are used for the velocity and pressure on the vertical sides of the domain. On the top the velocity components are free ($\partial u/\partial n = \partial v/\partial n = 0$), and the pressure is set to a fixed value. The anisotropy function for the interface energy is the same as Equation (35), and the kinetic mobility is constant.

We present two simulations, one with contraction and one without. The flows and the dendrites at two simulation times, 2.4 and 3.4s, are shown in Figures 13(a)–13(d). As expected the case without contraction exhibits thermosolutal convection as shown in Figures 13(a) and 13(c), where several convection cells can be seen ahead of the dendrite tips. Farther away from the dendrite tips convection is small because the concentration is almost uniform there. Interdendritic convection is seen at the earlier simulation time, Figure 13(a), when the dendrite spacings are large; near the roots of the dendrites the convection is minimal because the region is confined.

Figures 13(b) and 13(d) show the results of the case with contraction. The downward flow because of contraction is much stronger than the circulatory flow by thermosolutal buoyancy, and the latter is completely absorbed by the former. As a result, the flow is almost

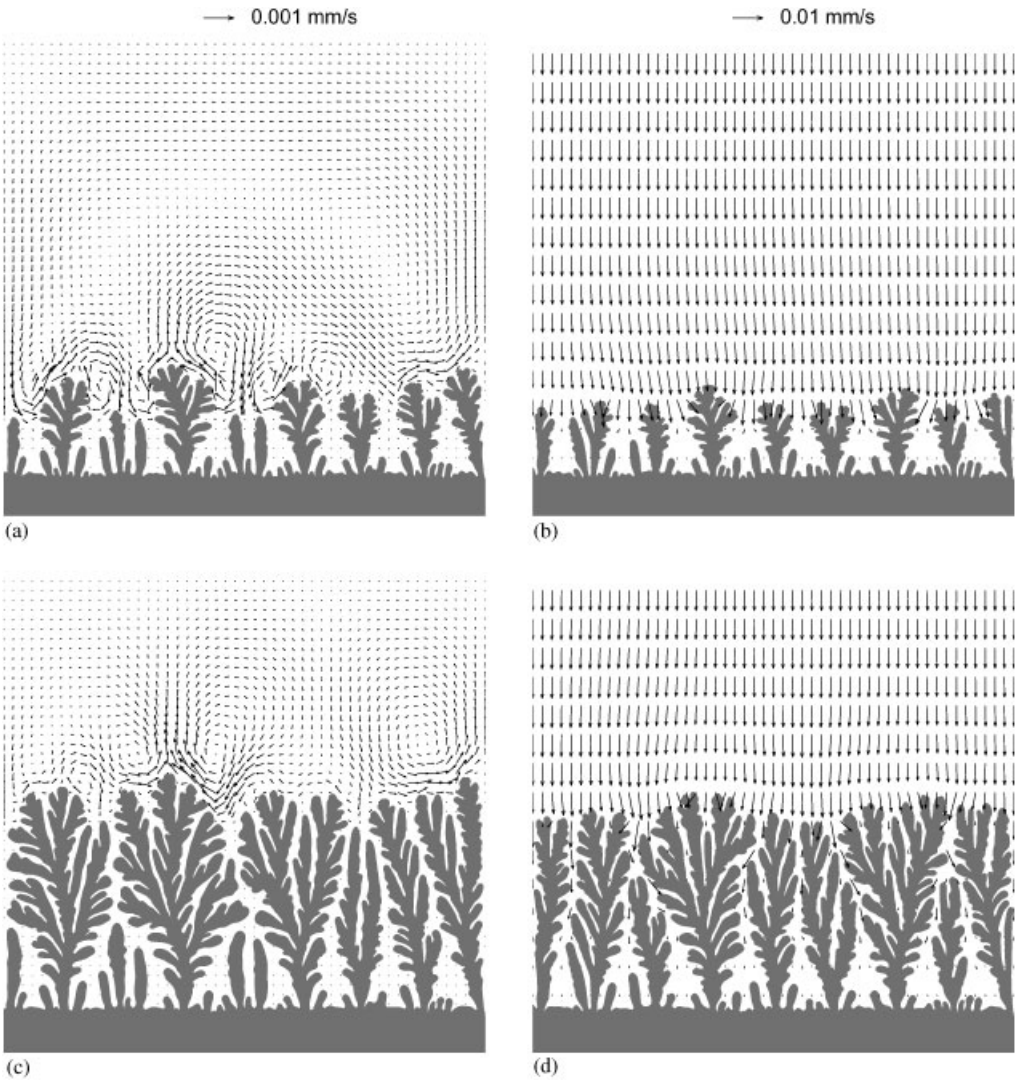

Figure 13. Dendrites and velocity vectors in directional solidification of Pb-0.2wt% Sb alloy with thermosolutal convection: (a) at $t = 2.4$ s without contraction; (b) at $t = 2.4$ s with contraction; (c) at $t = 3.4$ s without contraction; and (d) at $t = 3.4$ s with contraction.

unidirectional toward the dendrite zone and approximately one order of magnitude larger than the maximum velocity in the pure thermosolutal case. Note that the alloy used in this simulation has an initial (bulk) solute concentration of only 0.2 wt% Sb. If the initial concentration increases by one or two orders, solutal convection would be comparable or even stronger than contraction-induced convection. Richer alloys, however, are much more difficult to simulate [23, 24].

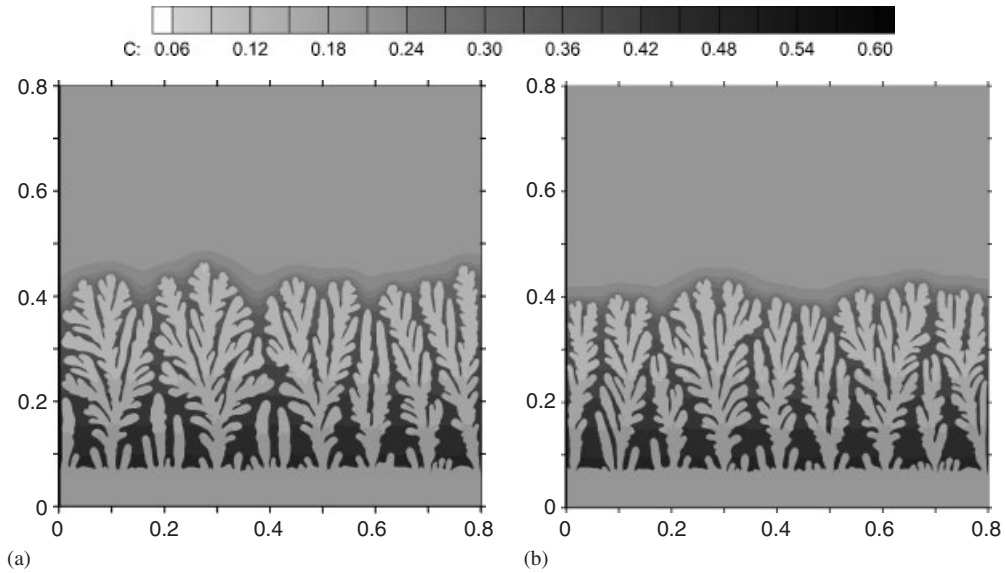

Figure 14. Solute concentration field (wt% Sb) at the end of simulation: (a) without contraction; and (b) with contraction. The dimension unit is mm.

The solutal concentration field is shown in Figures 14(a) and 14(b), where the solutal boundary layer can be seen ahead of the dendrite tips. Microsegregation can also be observed in the dendrites because the interface concentration at the root of the dendrites is higher than at the tip of the dendrites.

Figures 13 and 14 show a slight difference in solidification rate and dendritic structure. The first difference is that the dendritic growth in the case without contraction is slightly faster than that with contraction, because the almost unidirectional flow brings the hotter melt to the interface. This effect is opposite to that in the case presented in Section 5.3, where the contraction-induced convection carries the undercooled melt to the interface and enhances the solidification. The second difference is that the dendritic structure in the case with contraction is somewhat finer than without contraction. With contraction the interdendritic convection is stronger; this promotes the growth of those dendrites that tend to fall behind and the growth of side branches of the larger dendrites.

5. CONCLUSIONS

A sharp-interface finite element numerical model is presented for the simulation of dendritic solidification with free and forced convection. The model is an extension of the one developed in References [23, 24, 42] by including convection terms in the energy and solutal concentration equations and coupling the solution of the Navier–Stokes equations for incompressible flow. One of the advantages of this model is that it works directly with primitive parameters and can accommodate all forms of convection. To deal with the difficulties related to the solute segregation and the imposition of velocity boundary conditions at the interface,

a strategy is used that solves the concentration and Navier–Stokes equations in the liquid region only while solving the energy equation in the whole domain where the interface is explicitly tracked. Two meshes are used: a fixed one for the temperature and an adaptive one for the concentration and the flow fields. The adaptive mesh is locally refined in the vicinity of the interface to resolve the small length scales. The fixed mesh can also be non-uniform, with finer elements covering the region within which solidification takes place and coarser elements elsewhere. The flexibility associated with the meshes provides the advantage that simulations can be performed in a relatively large domain while keeping the number of elements relatively small. The major advantage of this model is that the imposition of the solute and velocity boundary conditions at the evolving interface is straightforward and easily handled; this is usually the biggest challenge for a pure Cartesian-grid method.

There are two drawbacks with this model, which have already been discussed in References [23, 24, 42]. The first one is related to the explicit tracking of the interface, which becomes complicated in three dimensions. This is a common drawback with any models that explicitly track the interface. It has been demonstrated, however, that in two dimensions the current interface-tracking method can resolve more complex interface morphologies than other explicit front-tracking methods [46]. The second drawback is the need to regenerate the adaptive mesh and to interpolate the field quantities from an old mesh to the new one. This is inevitable when adaptive meshes are used but is minimized by using a very efficient mesh generator [23].

The model without convection has been validated in References [23, 42]. The Navier–Stokes solver and the solution of convection–diffusion equations were tested in this article through several examples including uniform flow past a circular cylinder, flow around an oscillating circular cylinder and a Rayleigh–Benard thermal instability problem (See Appendix). Quantitative agreement is found between the results of this model and those of experiments, analysis and other calculations. Simulation results on crystal growth of succinonitrile with thermal convection are in excellent agreement with the results of Tönhardt and Amberg [6].

For the case of equiaxial dendritic growth into an undercooled pure melt with forced convection, the predicted dendritic tip velocities and radii compare very well to those reported by Beckermann *et al.* [9] and Al-Rawahi and Tryggvason [11]. Results on contraction-induced convection and alloy solidification with thermosolutal convection are new. It is found that convection due to contraction enhances the solidification rate and destabilizes the interface for both the undercooled pure substance and alloy considered. Simulations on directional solidification of a dilute Pb–Sb alloy show that thermosolutal convection cells develop ahead of the interface. For the dilute alloy, however, when contraction-induced convection was added, the thermosolutal convection cells disappear. The almost unidirectional flow caused by contraction in directional solidification slows down the solidification rate. Interdendritic convection tends to make the dendritic structure finer and more compact by promoting the growth of side branches and those dendrites that tend to be left behind.

APPENDIX A: MODEL VALIDATION

A series of model validation calculations is presented in our previous papers [23, 24, 42] for dendritic solidification of pure substances and alloys in the absence of convection. In Reference [42], the model shows second-order convergence in tracking the interface position and first

order in approximating the interface velocity for a two-dimensional solidification problem that permits exact solutions. For dendritic growth into an undercooled pure melt, the model was tested against solvability theory in predicting the tip growth velocity. For the case of binary alloys [23], the model again showed good accuracy in the temperature, solute concentration and the interface position and velocity for the test problems. The model predicted the onset of stability and unstable wavelengths in agreement with the linear stability theory of Mullins and Sekerka [50]. Mesh refinement studies were performed in References [42, 51]. In this section, we present validation of the model with three classical cases of convection.

A.1. Flow past a stationary circular cylinder

Flow past a circular cylinder has been a good model problem for flows past other shapes of bodies (including dendrites) and for validation of the Navier–Stokes solver. The physical problem becomes experimentally unstable with respect to unsymmetrical disturbances around Reynolds number $Re = 40$ based on the diameter of the cylinder and the free-stream velocity, U_∞. If symmetry is imposed, however, stability can persist for a much higher Re. Numerical studies for the steady symmetric problem of flow past a circular cylinder have been performed by, among others, Fornberg [52] who systematically studied the problem using a stream function-vorticity formulation. The positions of the end of the wake bubble for different Reynolds numbers are reported in Reference [52] and are used to test the current model.

Similar to Fornberg [52], we consider the upper-half plane since symmetry is assumed. The radius of the cylinder is $r = 1$, and the computational domain is a rectangle of 120×50 minus the half-cylinder at the origin as shown in Figure A1. The domain is chosen to be rather large to eliminate the influence of outer boundary conditions. The boundary conditions used in the calculations are shown in Figure A1. A mesh of about 94 000 nodes and 187 000 linear triangular elements is used. The mesh is body-fitted with refined elements around the cylinder and in the wake region behind the cylinder. On the half-cylinder surface 60 elements are used; the ratio of the coarsest element size (on the outer boundaries) to the finest element size (on the cylinder surface) is about 12. For this problem, the Reynolds number, $Re = 2U_\infty r/\nu$, is the only dimensionless parameter that determines the solutions. Calculations are performed for four different Reynolds numbers: $Re = 10$, 20, 40, and 100. The streamlines for these Reynolds

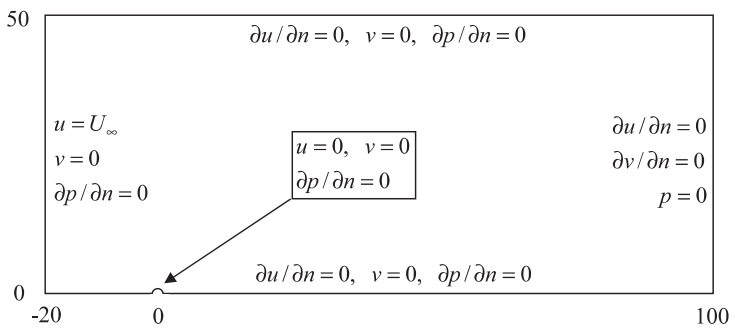

Figure A1. Computational domain for flow past a circular cylinder and the boundary conditions used in the calculations with the symmetry condition imposed. The half-cylinder resides at $(0, 0)$ with a radius of one unit.

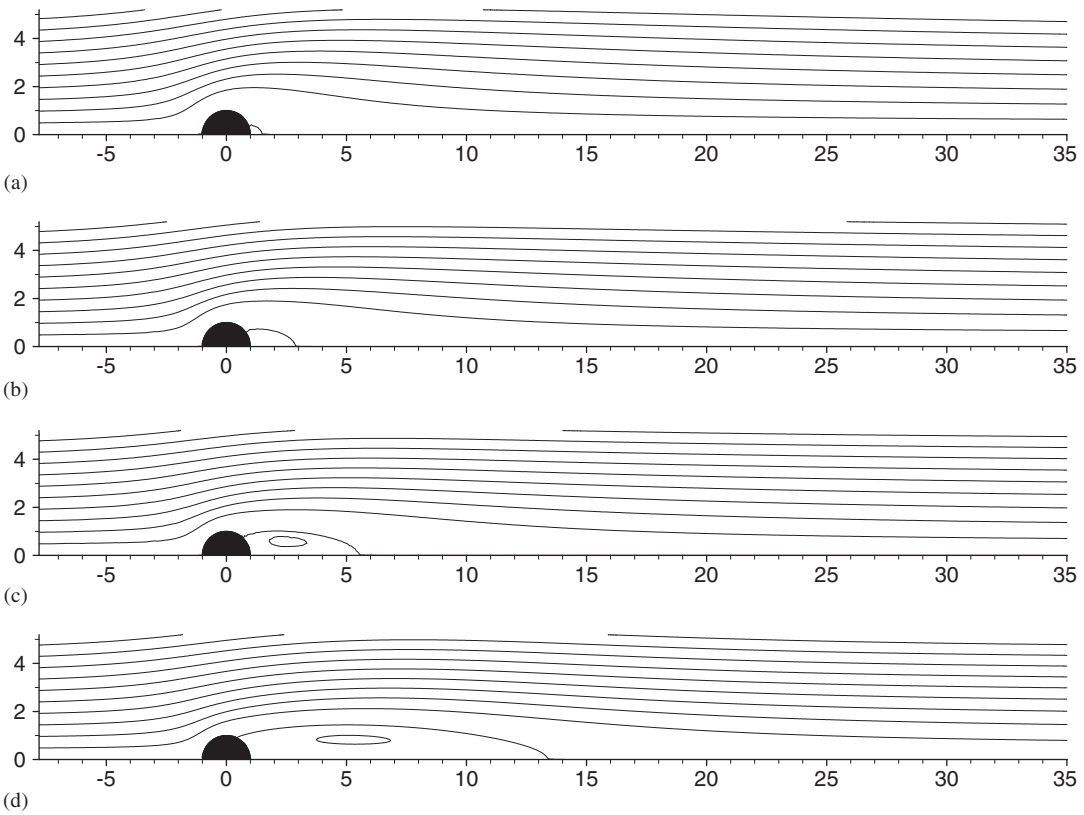

Figure A2. Flow past a circular cylinder: streamlines for (a) $Re = 10$; (b) $Re = 20$; (c) $Re = 40$; and (d) $Re = 100$.

Table AI. Position of end of wake bubble for different Reynolds numbers.

Re	10	20	40	100
Fornberg [52]	1.40	2.82	5.48	13.6
Current model	1.40	2.84	5.50	13.4

numbers are shown in Figures A2(a)–A2(d). The positions of the end of the wake bubble are listed in Table AI together with the results of Fornberg [52]; the differences are within 1.5%.

A.2. Flow induced by an oscillating circular cylinder

Flow induced by harmonic in-line oscillation of a circular cylinder in water at rest has been experimentally and numerically studied by Dütsch *et al.* [53]. Their experimental data and numerical results are in good agreement and are available for validation. Numerically, Dütsch *et al.* solved the problem using a second-order finite volume discretization in a non-inertial

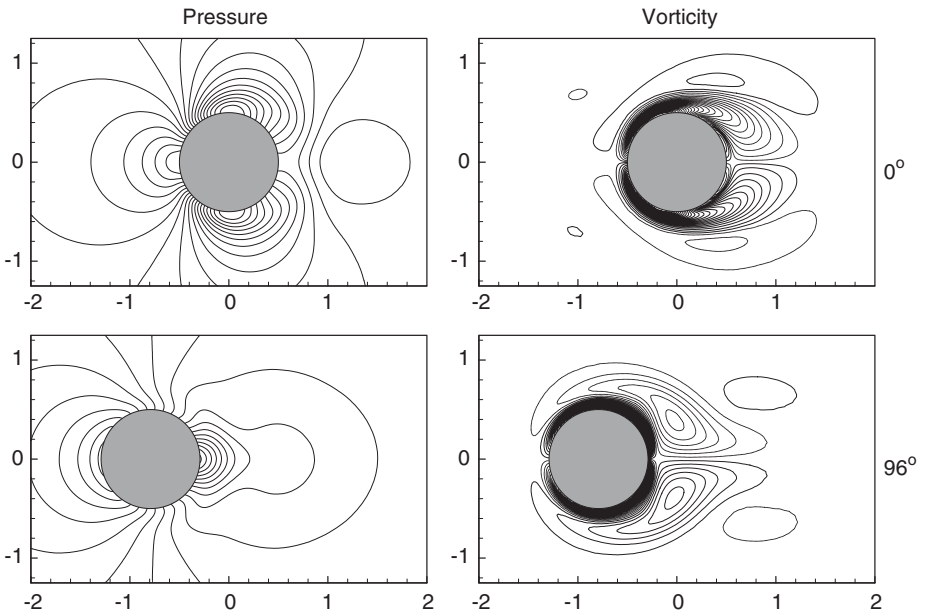

Figure A3. Pressure and vorticity at two phase angles, 0° and 96°, for $Re = 100$ and $KC = 5$.

system moving with the oscillating cylinder. An extra force term due to the system acceleration was added to the momentum equations and the problem was solved in a fixed grid. In order to test the current model for an adaptive mesh, the inertial system is used in our calculations, and the mesh changes every time step as the cylinder moves. The same parameters as those used by Dütsch *et al.* [53] are used. The cylinder, with a diameter of 1 cm, is placed at the centre of the computational domain, a square of 120×120 cm filled with water at rest. With such a large domain (compared to the dimension of the cylinder), the interactions between the outer boundaries and the cylinder are negligible. Flow induced by the cylinder oscillation is confined to the near-cylinder region.

The boundary conditions for velocity are: $\mathbf{u} = 0$ at the outer walls and $\mathbf{u} = \mathbf{V}_{\mathrm{cy}}(t)$ on the cylinder surface, where $\mathbf{V}_{\mathrm{cy}}(t)$ is the velocity of the cylinder. For pressure the following boundary conditions are used:

$$\frac{\partial p}{\partial n} = 0 \quad \text{on the outer walls, and}$$

$$\frac{\partial p}{\partial n} = -\left(\frac{D\mathbf{u}}{Dt}\right) \cdot \mathbf{n} = -\left(\frac{\mathrm{d}\mathbf{V}_{\mathrm{cy}}}{\mathrm{d}t}\right) \cdot \mathbf{n} \quad \text{on the cylinder surface}$$

A typical mesh consists of 60 000 nodes and 120 000 triangular elements with 200 elements on the cylinder surface. The mesh is graded, the elements are the finest near the cylinder and become coarser away from the cylinder. The ratio of the coarsest to the finest element sizes is around 80. To reduce the computational time for the mesh generation, the whole domain is divided into two regions: an inner region that encloses the cylinder and an outer region. The

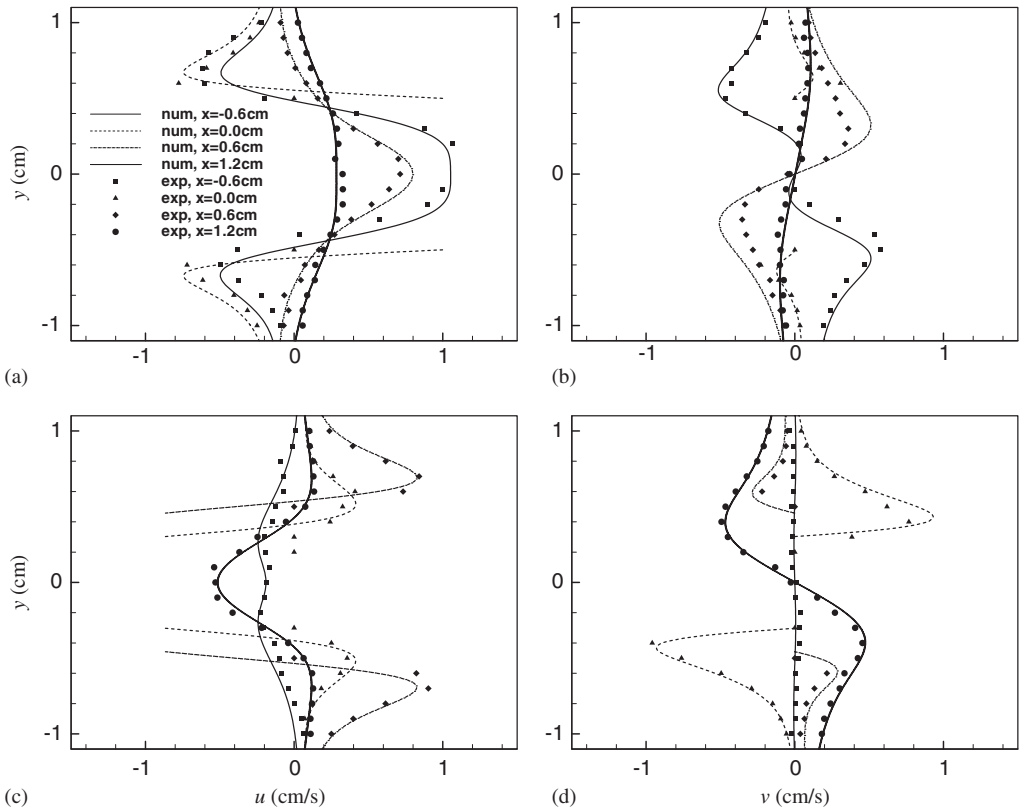

Figure A4. Comparison of velocity components between the numerical results by the current model and the experimental data by Dütsch *et al.* [53] at four cross-sections with constant x-value: (a) u at phase angle 180°; (b) v at 180°; (c) u at 330°; and (d) v at 330°. $Re = 100$ and $KC = 5$.

inner region moves with the cylinder, and the mesh on the inner region is fixed. The mesh that covers the outer region is adapted every time step. The whole mesh consists of the two meshes that merge.

The oscillation of the cylinder is given by $x(t) = -A\sin(2\pi ft)$, where $x(t)$ is the horizontal position of the cylinder, A and f denote the amplitude and frequency of the oscillation, respectively. For this problem, there are two independent dimensionless parameters, the Reynolds number $Re = U_{\max}D/v$ and the Keulegan–Carpenter number $KC = U_{\max}/fD$, where $U_{\max} = 2\pi fA$ is the maximum velocity of the cylinder and D is the diameter of the cylinder. Results for $Re = 100$ and $KC = 5$ are shown in Figures A3–A5. Figure A3 shows the pressure and vorticity in the vicinity of the cylinder for two phase-angles, 0° and 96°, of the oscillation; the patterns of the contours are in excellent agreement with those shown in Figure 6 of Reference [53]. Quantitative comparison with the experimental data by Dütsch *et al.* is shown in Figure A4 for the velocity components at four cross-sections for two phase angles. While the agreement is only reasonably good, the differences between the numerical results

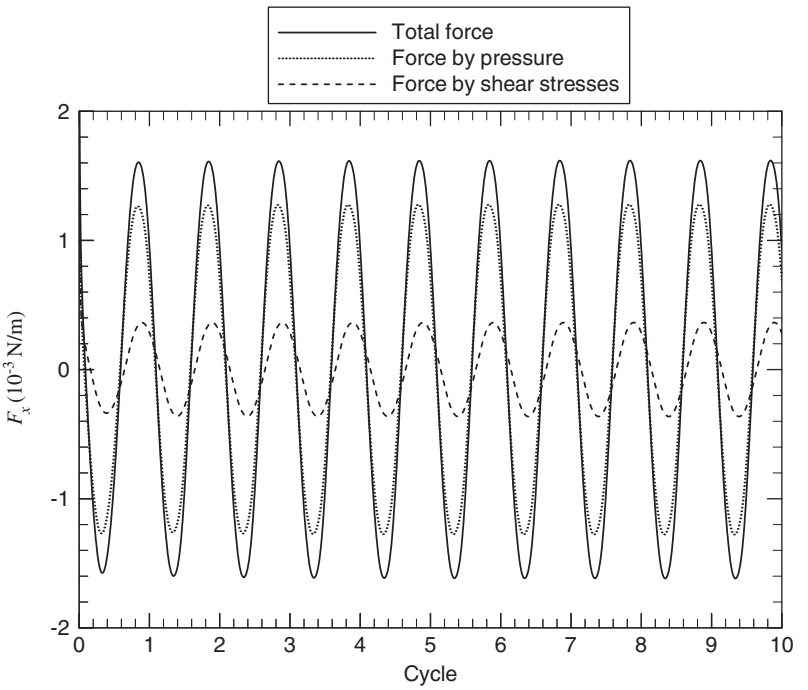

Figure A5. In-line force history for the first ten cycles, $Re = 100$ and $KC = 5$.

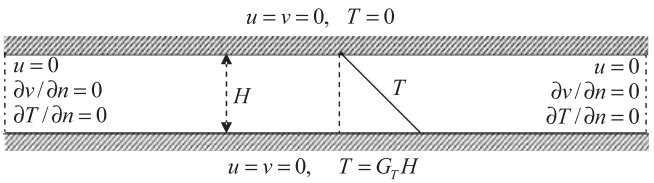

Figure A6. Computational domain ($8H \times H$) with boundary conditions used to simulate the thermal instability of a horizontal layer of fluid heated from below. The boundary condition for the pressure is $\partial p/\partial n = 0$ everywhere except one (arbitrary) point on the boundary.

and the experimental data shown in Figure A4 are almost identical to those shown in Figure 8 of Reference [53], indicating the two numerical results agree very well. Figure A5 shows the in-line force history, $F_x(t)$, for the first ten cycles of oscillation. By least-squares fitting to the following empirical formula [53],

$$F_x(t) = -c_d(\rho D\dot{x}|\dot{x}|/2) - c_i(\pi\rho D^2\ddot{x}/4)$$

where $\dot{x}$ and $\ddot{x}$ denote the first and second derivatives with respect to time, the drag and added-mass coefficients c_d and c_i are found to be 2.06 and 1.43, respectively, compared to the results of Dütsch *et al.* of 2.09 and 1.45, respectively.

A.3. The Bénard thermal instability problem

The thermal instability of a horizontal layer of fluid heated from below is considered to test whether the current model captures the onset of the instability and convection beyond the onset. The fluid layer is initially at rest with a constant adverse temperature gradient, G_T, imposed in the gravitational direction. The only dimensionless parameter that determines the onset of stability of the fluid layer is the Rayleigh number, $R_T = gH^4\beta_T G_T/\nu\alpha_L$, with H being the height of the fluid layer. According to the hydrodynamic stability theory, the critical value of R_T, at which instability sets in, is 1708 for rigid top and bottom boundaries. The convection cells at the marginal state have a dimensionless wave length of 2.016 based on the height of the layer. The theoretical results are based on the assumption that the horizontal dimension of the layer is infinite. To simulate this problem with the current model, a domain of 8×1 is used as shown in Figure A6 with the boundary conditions indicated. Simulations show that no convection develops for Rayleigh number(R_T) up to 1700. The minimum R_T considered at which steady convection appeared is 1718, very close to the critical value 1708 predicted by theory. (Rayleigh numbers between 1708 and 1718 have also been tried, and convection does appear after a sufficiently long time of simulation. The convection, however, is very weak and strongly influenced by numerical noise). At $R_T = 1718$, there appear eight convection cells in the 8×1 channel, indicating the calculated wavelength is 2 (one wavelength contains two cells).

Table AII. Variation of the Nusselt number with the Rayleigh number.

R_T	1700	2000	3000	4000	8000	16 000	30 000
Nu	1.000	1.180	1.645	1.915	2.452	2.954	3.474

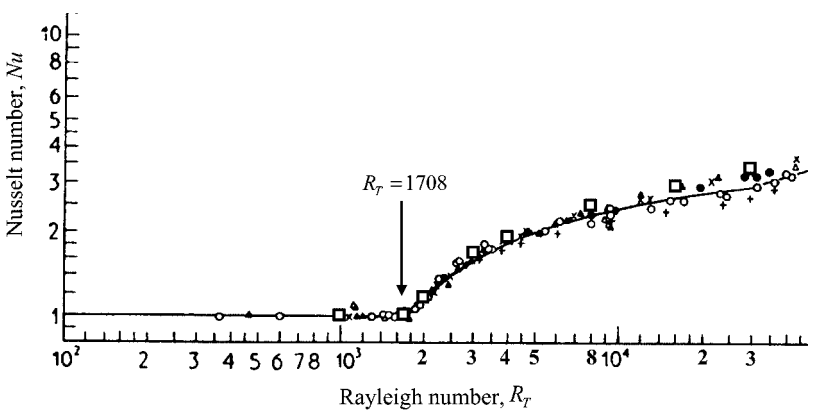

Figure A7. The Nusselt number against the Rayleigh number. The plot is a direct copy from Figure 13 of Reference [49]. Current numerical results, denoted by the open squares, are added. Other symbols are experimental results for different liquids.

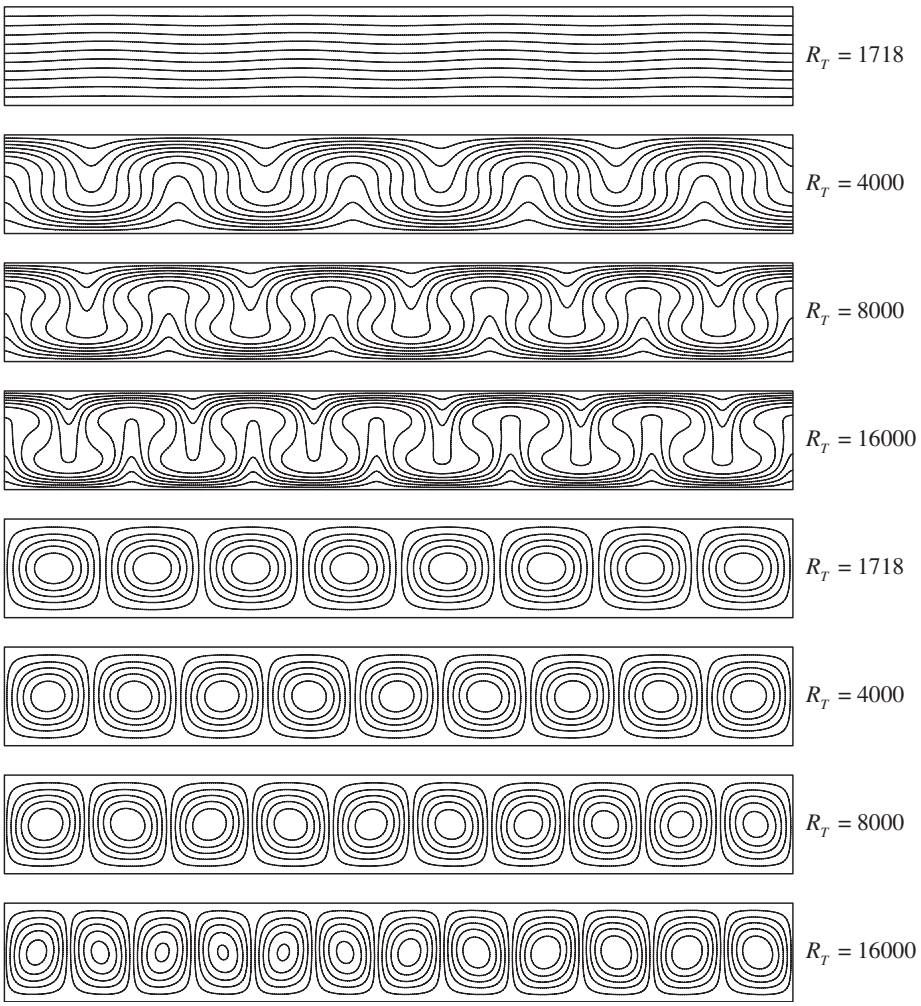

Figure A8. Temperature and stream functions for four different Rayleigh numbers.

For R_T beyond the critical number, simulations were performed for $R_T = 2000$, 3000, 4000, 8000, 16 000, and 30 000. For each of these Rayleigh numbers, the Nusselt number, defined as $Nu = q/\kappa G_T$ with q being the heat flux on the boundary surface, is calculated. The calculated Nusselt number versus the Rayleigh number is listed in Table AII and plotted in Figure A7 together with the experimental data reported in Figure 13 of Reference [49]. The comparison shows good agreement between the numerical and experimental results. Figure A8 shows the temperature and stream function isolines for four different Rayleigh numbers. It is seen that as R_T increases, the distortion of temperature isolines from the base state (horizontal lines) increases and the number of the convection cells increases, indicating that the active convection wavelength becomes shorter and the convection becomes stronger. It is also found

that the Prandtl number has a very small effect on the Nusselt number; this is also indicated by the experimental results reported in Reference [49].

Based on these results, the present model was determined to be appropriate for simulating solidification/convection problems.

ACKNOWLEDGEMENTS

This work was supported by the National Aeronautics and Space Administration under Grant NCC8-96 and by the National Science Foundation under Grant DMR 0072955.

REFERENCES

1. Flemings MC. *Solidification Processing*. McGraw-Hill, Inc.: New York, 1974; 214.
2. Glicksman ME, Huang SC. Convective heat transfer during dendritic growth. In *Convective Transport and Instability Phenomena*, Zierep J, Oertel H (eds). Karlsruhe: Braun, 1982; 557.
3. Lee YW, Smith RN, Clicksman ME, Koss MB. Effects of buoyancy on the growth of dendritic crystals. In *Annual Review of Heat Transfer*, vol. 7, Tien CL (ed.). Begell House: New York, 1996; 59.
4. Tewari SN, Shah R. Macrosegregation during steady-state arrayed growth of dendrites in directionally solidified Pb–Sn alloys. *Metallurgical Transaction A* 1992; **23A**(12):3383–3392.
5. Tewari SN, Shah R. Macrosegregation during dendritic arrayed growth of hypoeutectic Pb–Sn alloys: Influence of primary arm spacing and mushy zone length. *Metallurgical and Material Transactions A* 1996; **27A**(5): 1353–1362.
6. Tönhardt R, Amberg G. Simulation of natural convection effects on succinonitrile crystals. *Physical Review E* 2000; **62**:828–836.
7. Tönhardt R, Amberg G. Phase-field simulation of dendritic growth in a shear flow. *Journal of Crystal Growth* 1998; **194**:406–425.
8. Tönhardt R, Amberg G. Dendritic growth of randomly oriented nuclei in a shear flow. *Journal of Crystal Growth* 2000; **213**:161–187.
9. Beckermann C, Diepers HJ, Steinbach, Karma IA, Tong X. Modeling melt convection in phase-field simulations of solidification. *Journal of Computational Physics* 1999; **154**:468–496.
10. Tong X, Beckermann C, Karma A, Li Q. Phase field simulation of dendritic crystal growth in a forced flow. *Physical Review E* 2000; **63**(1–16):061601.
11. Al-Rawahi N, Tryggvason G. Numerical simulation of dendritic solidification with convection: two-dimensional geometry, *Journal of Computational Physics* 2002; **180**:471–496.
12. Udaykumar HS, Marella S, Krishnan S. Sharp-interface simulation of dendritic growth with convection: benchmarks. *International Journal of Heat and Mass Transfer* 2003; **46**:2615–2627.
13. Jeong JH, Goldenfeld N, Dantzig JA. Phase field model for three-dimensional dendritic growth with fluid flow. *Physical Review E* 2001; **64**(1–14):041602.
14. Jeong JH, Dantzig JA, Goldenfeld N. Dendritic growth with fluid flow in pure materials. *Metallurgical and Material Transaction A* 2003; **34**:459–466.
15. Boettinger WJ, Warren JA, Beckermann C, Karma A. Phase-field simulation of solidification. *Annual Review of Material Research* 2001; **32**:163–194.
16. Al-Rawahi N, Tryggvason G. Numerical simulation of dendritic solidification with convection: three-dimensional flow. *Journal of Computational Physics* 2004; **194**:677–696.
17. Lan CW, Shih JC. Efficient phase field simulation of a binary dendritic growth in a forced flow. *Physical Review E* 2004; **69**(1–10):031601.
18. Bänsch E, Schmidt A. Simulation of dendritic crystal growth with thermal convection. *Interfacial Free Boundaries* 2000; **2**:95–115.
19. Ananth R, Gill WN. Dendritic growth with thermal-convection. *Journal of Crystal Growth* 1988; **91**:587–598.
20. Coriell SR, McFadden GB, Mitchell WF, Murray BT, Andrews JB, Arikawa Y. Effect of flow due to density change on eutectic growth. *Journal of Crystal Growth* 2001; **224**:145–154.
21. Jackson KA, Hunt JD. Lamellar and rod eutectic growth. *Transactions on TMS-AIME* 1966; **236**:1129–1142.
22. Conti M. Advection flow effects in the growth of a free dendrite. *Physical Review E* 2004; **69**(1–4):022601.
23. Zhao P, Venere M, Heinrich JC, Poirier DR. Modeling dendritic growth of a binary alloy. *Journal of Computational Physics* 2003; **188**:434–461.
24. Zhao P, Heinrich JC, Poirier DR. Stability of numerical simulations of dendritic solidification. *JSME International Journal Series B* 2003; **46**:586–592.

25. Peskin CS. Numerical analysis of blood flow in the heart. *Journal of Computational Physics* 1977; **25**: 220–252.
26. Goldstein D, Handler R, Sirovich L. Modeling a no-slip flow boundary with an external force field. *Journal of Computational Physics* 1993; **105**:354–366.
27. Fadlun EA, Verzicco R, Orlandi P, Mohd-Yusof J. Combined immersed boundary finite-difference methods for three-dimensional complex flow simulations. *Journal of Computational Physics* 2000; **161**:35–60.
28. Gilmanov A, Sotiropoulos F, Balaras E. A general reconstruction algorithm for simulating flows with complex 3D immersed boundaries on Cartesian grids. *Journal of Computational Physics* 2003; **191**:660–669.
29. Ye T, Mittal R, Udaykumar HS, Shyy W. An accurate Cartesian grid method for viscous incompressible flows with complex immersed boundaries. *Journal of Computational Physics* 1999; **156**:209–240.
30. Udaykumar HS, Mittal R, Rampunggoon P, Khanna A. A sharp interface Cartesian grid method for simulating flows with complex moving boundaries. *Journal of Computational Physics* 2001; **174**:345–380.
31. Chang CJ, Brown RA. Finite element calculation of buoyancy-driven convection near a melt/solid phase boundary. In *Numerical Properties and Methodologies in Heat Transfer*, Shih TM (ed.). Hemisphere: New York, 1983; 283–304.
32. Kang IS, Leal LG. Numerical-solution of axisymmetrical, unsteady free-boundary problems at finite Reynolds-number. 1. Finite-difference scheme and its application to the deformation of a bubble in a uniaxial straining flow. *Physics of Fluids* 1987; **30**:1929–1940.
33. Shyy W, Udaykumar HS, Rao MM, Smith RW. *Computational Fluid Dynamics with Moving Boundaries*. Hemisphere: Washington, DC, 1996; 61.
34. Yeoh GH, de Vahl Davis G, Leonardi E, de Groh III HC, Yao M. A numerical and experimental study of natural convection and interface shape in crystal growth. *Journal of Crystal Growth* 1997; **173**:492–502.
35. Dari EA, Buscaglia G. Topics on finite element meshes for problems with moving boundaries. In *Finite Elements in Fluids. New Trends and Applications*, *Part I*, Morgan K, Oate E, Periaux J, Peraire J, Zienkiewicz OC (eds). CIMNE: Barcelona, 1993; 726–735.
36. Löhner R. Adaptive meshing for transient problems. *Computer Methods in Applied Mechanics and Engineering* 1989; **75**:195–214.
37. Provatas N, Goldenfeld N, Dantzig J. Adaptive mesh refinement computation of solidification microstructures using Dynamic data structure. *Journal of Computational Physics* 1999; **148**:265–290.
38. Pember RB, Bell JB, Colella P, Curtchfield WY, Welcome ML. An adaptive Cartesian grid method for unsteady compressible flow in irregular regions. *Journal of Computational Physics* 1995; **120**:278–304.
39. Lan CW, Liu CC, Hsu CM. An adaptive finite volume method for incompressible heat flow problems in solidification. *Journal of Computational Physics* 2002; **178**:464–497.
40. Russell D, Wang ZJ. A Cartesian grid method for modeling multiple moving objects in 2D incompressible viscous flow. *Journal of Computational Physics* 2003; **191**:177–205.
41. Linnick MN. A high order immersed boundary method for unsteady incompressible flow calculations. *Ph.D. Dissertation*, The University of Arizona, Tucson, Arizon, 2003; 107.
42. Zhao P, Heinrich JC. Front-tracking finite element method for dendritic solidification. *Journal of Computational Physics* 2001; **173**:765–796.
43. Padra C, Vénere MJ. On adaptivity for diffusion problems using triangular elements. *Engineering Computations* 1995; **12**:75–84.
44. Rivara MC, Vénere MJ. Cost analysis of the longest-side refinement algorithm for triangulations. *Engineering Computations* 1996; **12**:224–234.
45. Dari EA, Vénere MJ. A node replacement method for automatic mesh generation. *Latin American Applied Research* 1991; **21**:275–282.
46. Zhao P, Heinrich JC, Poirier DR. Fixed mesh front-tracking methodology for finite element simulations. *International Journal for Numerical Methods in Engineering* 2004; **61**:928–948.
47. Alexiades V, Solomon AD. *Mathematical Modeling of Melting and Freezing Processes*. Hemisphere Publishing Corp.: Washington, DC, 1993; 92.
48. Juric D, Tryggvason G. A front-tracking method for dendritic solidification. *Journal of Computational Physics* 1996; **123**:127–148.
49. Chandrasekhar S. *Hydrodynamic and Hydromagnetic Stability*. Dover Publications, Inc.: New York, 1961; Chapter 2.
50. Mullins WW, Sekerka RF. Stability of planar interface during solidification of dilute binary alloy. *Journal of Applied Physics* 1964; **35**:444–451.
51. Zhao P, Heinrich JC. Numerical approximation of a thermally driven interface using finite elements. *International Journal for Numerical Methods in Engineering* 2003; **56**:1533–1547.
52. Fornberg B. A numerical study of steady viscous flow past a circular cylinder. *Journal of Fluid Mechanics* 1980; **98**:819–855.
53. Dütsch H, Durst F, Becker S, Lienhart H. Low-Reynolds-number flow around an oscillating circular cylinder at low Keulegan–Carpenter numbers. *Journal of Fluid Mechanics* 1998; **360**:249–271.

